



# Temperatures in the Upper Mesosphere and Lower Thermosphere from O<sub>2</sub> Atmospheric Band Emission Observed by ICON/MIGHTI

M.H. Stevens<sup>1</sup> · C.R. Englert<sup>1</sup> · J.M. Harlander<sup>2</sup> · K.D. Marr<sup>1</sup> · B.J. Harding<sup>3</sup> · C.C. Triplett<sup>3</sup> · M.G. Mlynczak<sup>4</sup> · T. Yuan<sup>5</sup> · J.S. Evans<sup>6</sup> · S.B. Mende<sup>3</sup> · Thomas J. Immel<sup>3</sup>

Received: 28 April 2022 / Accepted: 31 October 2022 / Published online: 21 November 2022

This is a U.S. Government work and not under copyright protection in the US; foreign copyright protection may apply 2022

## Abstract

The Michelson Interferometer for Global High-resolution Thermospheric Imaging (MIGHTI) was launched aboard NASA's Ionospheric Connection (ICON) Explorer satellite in October 2019 to measure winds and temperatures on the limb in the upper mesosphere and lower thermosphere (MLT). Temperatures are observed using the molecular oxygen atmospheric band near 763 nm from 90–127 km altitude in the daytime and 90–108 km in the nighttime. Here we describe the measurement approach and methodology of the temperature retrieval, including unique on-orbit operations that allow for a better understanding of the instrument response. The MIGHTI measurement approach for temperatures is distinguished by concurrent observations from two different sensors, allowing for two self-consistent temperature products. We compare the MIGHTI temperatures against existing MLT spaceborne and ground-based observations. The MIGHTI temperatures are within 7 K of these observations on average from 90–95 km throughout the day and night. In the daytime on average from 99–105 km, MIGHTI temperatures are higher than coincident observations by the Sounding of the Atmosphere using Broadband Emission Radiometry (SABER) instrument on NASA's TIMED satellite by 18 K. Because the difference between the MIGHTI and SABER observations is predominantly a constant bias at a given altitude, conclusions of scientific analyses that are based on temperature variations are largely unaffected.

**Keywords** ICON · MIGHTI · Temperature · Mesosphere · Thermosphere

---

The Ionospheric Connection Explorer (ICON) Mission: First Results  
Edited by David E. Siskind and Ruth S. Lieberman

---

✉ M.H. Stevens  
[michael.stevens@nrl.navy.mil](mailto:michael.stevens@nrl.navy.mil)

<sup>1</sup> Space Science Division, U.S. Naval Research Laboratory, Washington, DC, USA

<sup>2</sup> Space Systems Research Corporation, Alexandria, VA, USA

<sup>3</sup> Space Sciences Laboratory, University of California, Berkeley, CA, USA

<sup>4</sup> NASA Langley Research Center, Langley, VA, USA

<sup>5</sup> Center for Atmospheric and Space Sciences, Utah State University, Logan, UT, USA

<sup>6</sup> Computational Physics, Inc., Springfield, VA, USA

## 1 Introduction

Understanding the coupling of the earth's lower atmosphere with the space environment has been a topic of focused research in recent years (*e.g.* Sagawa et al. 2005; Hagan et al. 2007; Immel et al. 2009; England 2012). Central to this understanding is the boundary region around 100 km, where upward propagating tidal oscillations and in situ tidal oscillations are comparable in magnitude (*e.g.* Forbes 1982). One useful way to advance our understanding of this region is through global-scale temperature observations from a space-based platform.

The NASA Ionospheric Connection (ICON) Explorer mission was launched in October 2019 with the overarching goal of understanding the connection between the lower atmosphere and the space environment (Immel et al. 2018). The Michelson Interferometer for Global High-resolution Thermospheric Imaging (MIGHTI) aboard ICON uses the innovative technique of Doppler Asymmetric Spatial Heterodyne Spectroscopy (DASH; Englert et al. 2007; Harlander et al. 1992) to observe the upper mesosphere and lower thermosphere (MLT). MIGHTI measures altitude profiles of horizontal neutral winds and neutral temperatures in the earth's MLT (Englert et al. 2017; Harding et al. 2017; Stevens et al. 2018; Harding et al. 2021).

MIGHTI obtains MLT temperatures by imaging the limb near the wavelength of 763 nm to observe the molecular oxygen ( $\text{O}_2$ )  $b^1\Sigma_g^+(0) - X^3\Sigma_g^-(0)$  atmospheric band (hereafter "A-band"), which is a bright airglow feature peaking near 85 km. The rotational distribution of the A-band is temperature dependent and can readily be used to measure MLT temperatures (*e.g.* Skinner and Hays 1985; Heller et al. 1991; Christensen et al. 2013; Kaufmann et al. 2018; Gumbel et al. 2020). Sheese et al. (2010) used limb observations of the A-band by the Optical Spectrograph and InfraRed Imaging System (OSIRIS) on the Odin satellite to retrieve temperatures between 90 and 110 km from 2002–2012 at a fixed local time (LT) near the terminator.

MIGHTI complements the OSIRIS observations by measuring the A-band over the entire diurnal cycle by virtue of ICON's orbital precession, thereby allowing us to quantify the tidal oscillations prevalent in this altitude region. In addition, MIGHTI temperatures are reported from two different sensors that separately measure the same volume of air nine minutes apart, enabled by operations for MIGHTI wind observations made simultaneously (Englert et al. 2017). This redundancy allows for self-consistent temperature datasets in this highly variable boundary region of the atmosphere.

An earlier study based on MIGHTI pre-launch sensor specifications determined the expected precision of local MLT temperature observations using its three signal channels observing the A-band and two background channels (Stevens et al. 2018). The present study is motivated by the wealth of MIGHTI observations acquired on-orbit that have enabled us to better determine the sensor performance and optimize the retrieval algorithm. Here we show how these observations are used to derive temperature profiles in the earth's MLT and compare results from both MIGHTI sensors to other MLT temperature datasets.

This manuscript is organized in the following way: Sect. 2 briefly describes the ICON/MIGHTI observations, including the latitude and LT coverage, as well as the spectral coverage of the A-band. Section 3 shows an example of data collected on-orbit and describes how we have modified pre-flight calibration results using on-orbit Rayleigh scattering observations in the MIGHTI background channels. This Section also discusses and quantifies the effects of possible contaminating features within the MIGHTI passbands. Section 4 describes the temperature retrieval and compares retrieved temperature profiles between MIGHTI-A and MIGHTI-B. Section 5 compares MIGHTI temperature profiles against those from concurrent satellite and ground-based datasets. Section 6 discusses some implications of the MIGHTI temperature results and Sect. 7 summarizes the work.

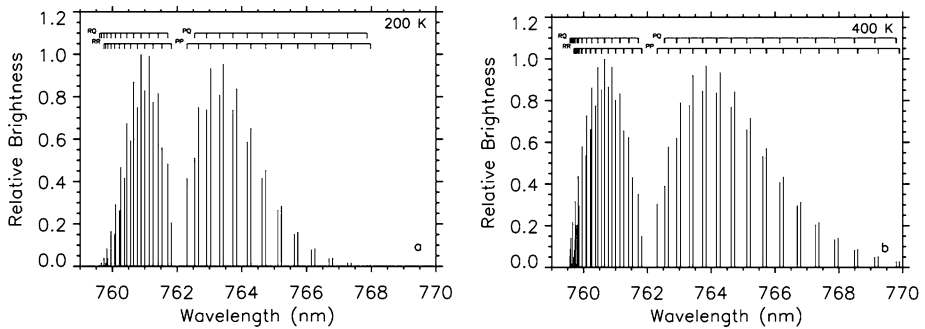


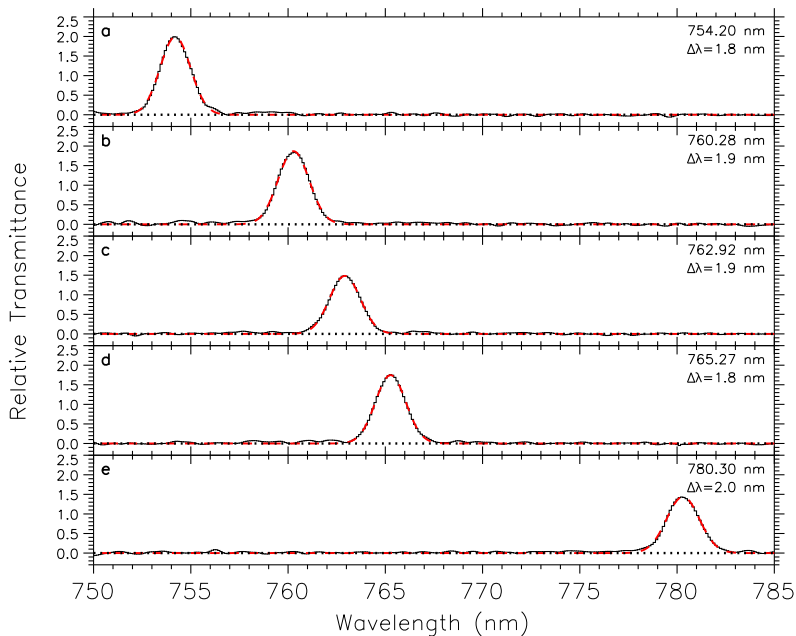
**Fig. 1** (a) Relative brightnesses of individual rotational lines in the O<sub>2</sub> A (0,0) band at 200 K. The four branches are labeled and transitions within each branch indicated. (b) Same as Fig. 1a but at 400 K

## 2 The ICON/MIGHTI Temperature Observations

### 2.1 The MIGHTI Measurement Concept

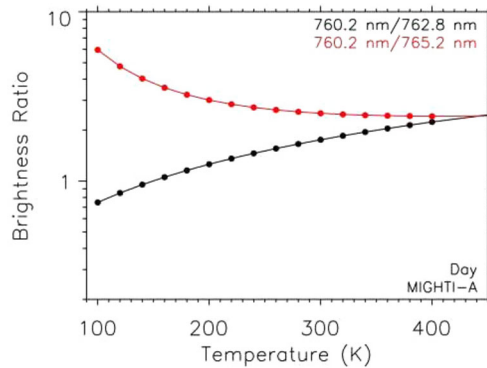
MIGHTI images the limb from ICON at discrete infrared wavelengths chosen specifically to capture the temperature dependent spectral shape of the O<sub>2</sub> A (0,0) band that emits from 759–770 nm in the MLT. The MIGHTI measurement approach employs five different filters around the A-band, each of them with a full-width at half-maximum of about 2 nm. Three of them are located on the band itself and two of them are located on either side of the band to quantify any background signal that might be present. The two background channels are placed at wavelengths near 754.2 nm and 780.3 nm to minimize contributions from any contaminating features (Christensen et al. 2012; Stevens et al. 2018). Although only two signal channels are theoretically necessary to retrieve the temperature, the three signal channels and two background channels used in both MIGHTI sensors provide valuable additional information used to monitor the instrument performance and better constrain the temperature retrieval, as we will show.

Figure 1a shows the O<sub>2</sub> A-band spectrum at 200 K, given by the relative line strengths in the High Resolution Transmission database (HITRAN2016; Gordon et al. 2017). Figure 1a shows the line strengths weighted by the temperature dependent partition function. For the temperature retrieval the lines are combined with a sampling of  $1.35 \times 10^{-4}$  nm, which is fine enough to resolve the Doppler broadened width. The A-band is described by two R branches and two P branches (Babcock and Herzberg 1948). Isotopic lines are over two orders of magnitude weaker (Gordon et al. 2017) but are included in the analysis. The MIGHTI temperature measurement is motivated by the fact that the rotational envelope of this band changes with temperature such that at higher temperature, higher rotational levels are populated and the shape of the band broadens. This is shown in Fig. 1b, which demonstrates that more rotational lines are discernible at 400 K than at 200 K. The two temperatures used in Figs. 1a and 1b approximately represent the two extremes expected in the earth's MLT at mid-latitudes. The three MIGHTI signal channels at 760.3 nm, 762.9 nm, and 765.3 nm are spectrally located to maximize the sensitivity to the changes shown in Fig. 1 (Stevens et al. 2018). Because the temperature information is contained in the shape of the spectrum rather than its magnitude, the relative calibration of the signal channels is sufficient, and an absolute radiometric calibration of the signal channels is not required for the retrieval.



**Fig. 2** (a) Measured filter function for the bottom row in the center of the MIGHTI-A daytime background channel peaking at 754.20 nm. The fitted Gaussian function is overlotted in red, with the calculated width indicated. (b) Same as Fig. 2a except for the bottom center of the MIGHTI-A daytime signal channel near 760.28 nm. (c) Same as Fig. 2a except for the bottom center of the MIGHTI-A daytime signal channel near 762.92 nm. (d) Same as Fig. 2a except for the bottom center of the MIGHTI-A daytime signal channel near 765.27 nm. (e) Same as Fig. 2a except for the bottom center of the MIGHTI-A daytime background channel near 780.30 nm

Each image of Level 1 MIGHTI data is made up of a two-dimensional array of pixels. For each of the infrared signal channels measuring the A-band on the limb, this array is described by 52 pixels horizontally by 18 pixels (rows) vertically. The filter passband for each of these pixels was measured prior to launch in the laboratory for the three signal channels and in the two background channels in each sensor for both daytime and nighttime configuration. Examples of filter passbands for the five MIGHTI channels are shown in Figs. 2a-2e. They are well approximated by a Gaussian. Figures 2a-2e show that the measured wings of the filter passbands do not quite reach zero and typically have larger values than the fitted Gaussian functions used in the retrieval, also shown in the panels. This difference persists far away from the transmission peaks of the filters and is an artifact of the measurements that are expressed as the positive definite amplitude spectra determined from a Fourier Transform Spectrometer. The fits in Figs. 2a-2e therefore do not have a constant term to account for this small offset so that each Gaussian is fit with an amplitude, a peak wavelength, and a width. Laboratory measurements of the filter passbands were sampled at  $2 \text{ cm}^{-1}$  ( $\sim 0.1 \text{ nm}$ ), but these measurements were interpolated onto a finer  $0.2 \text{ cm}^{-1}$  grid for fitting, due to the extreme sensitivity of the temperature measurements to the peak wavelength of the fitted Gaussian. The smooth Gaussians are then averaged over the pixels for each channel and in each row to determine an average peak wavelength and a relative responsivity for each channel and row. This is repeated for the daytime and nighttime configuration as well as for the MIGHTI-A and MIGHTI-B sensors at a variety of temperatures, so that there are four different calibration files used for quantifying the sensor response of the MIGHTI observations.



**Fig. 3** Two brightness ratios of A-band emission from the three MIGHTI-A signal channels using HITRAN2016 spectra at the indicated temperatures and pre-flight responsivities measured in daytime mode. The ratios are from the fourth row of MIGHTI, which is at approximately 100 km tangent point height for nominal viewing conditions. The brightness ratios are a strong function of temperature and wavelength as shown, but also depend on the sensor (A or B), the mode of operation (night or day), the relative responsivity of each channel (wavelength), and sensor row (altitude)

Figure 3 demonstrates the sensitivity of MIGHTI to typical upper atmospheric temperatures at the bottom row of the MIGHTI-A sensor (nominally corresponding to a field-of-view tangent height of 90 km). Here we have convolved the A-band with the average filter functions for each signal channel and taken two channel ratios. Wavelengths indicated represent the average at the peak of the fitted Gaussian (Fig. 2) over all the signal channel pixels. Figure 3 shows that the channel ratios can readily determine changes in the upper atmospheric temperature. The average filter functions are applied to the HITRAN2016 output (Fig. 1) at a variety of different temperatures to show the response of the instrument to temperature changes in the observed atmosphere. The temperature dimension of the calibration matrices is as shown in Fig. 3, with interpolation over 20 K steps between 100 K and 400 K and 100 K steps above 400 K. The temperature sampling is empirically determined, and results from a balance between retrieval speed and required accuracy.

We collectively refer to the measured responsivities and wavelengths of all the MIGHTI channels as the flat fields. We have made modifications to both the daytime and nighttime pre-launch flat fields for MIGHTI-A and MIGHTI-B channels at observed altitudes using on-orbit observations of Rayleigh scattered light from the earth's limb in the background channels. These modifications will be discussed in Sect. 3.

## 2.2 On-Orbit Operations

The ICON satellite launched with a Pegasus XL rocket on 11 October 2019 at 01:59:45 UT and the satellite was placed into a near circular orbit with altitude  $\sim 600$  km at a  $27^\circ$  inclination. The MIGHTI instrument has two telescopes, which point northward at  $45^\circ$  and  $135^\circ$  in azimuth from the velocity vector of the spacecraft (Englert et al. 2017). In this way MIGHTI-A typically images nearly the same volume of air at the tangent point nine minutes before MIGHTI-B. These operations enable the retrieval of the zonal and meridional winds (Harding et al. 2017), but also allow for redundant temperature datasets at nearly the same time and location.

Although the entire MIGHTI field of view subtends the equivalent of approximately 210 km vertically on the limb to include observations of the atomic oxygen green line and

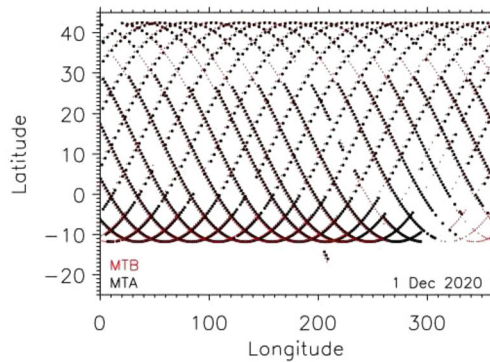


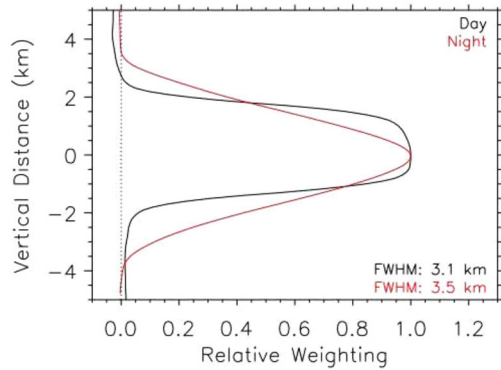
**Fig. 4** Tangent altitude ground tracks for the bottom row of a day of MIGHTI-A (black) and MIGHTI-B (red) images on 1 December 2020. More closely spaced images are taken during the day (30 s exposures) and more separated images are taken during the night (60 s exposures). MIGHTI-B images are obtained nine minutes after MIGHTI-A images at a given geographical location. There are gaps near the morning terminator as MIGHTI switches from night operations to day operations (see text). MIGHTI is sensitive to enhanced particle precipitation in the South Atlantic Anomaly (bottom right), rendering A-band observations unretrievable, so these are removed from processing

red line emissions for the wind measurements (Englert et al. 2017; Harding et al. 2017), the A-band images only subtend approximately 50 km vertically. The MIGHTI telescopes are oriented so that the bottom of the MIGHTI-A and MIGHTI-B sensors are observing at a tangent altitude of 90 km during both daytime and nighttime operations. Retrieved daytime and nighttime temperature profiles therefore have a minimum altitude of 90 km but the maximum altitude is different for daytime (127 km) and nighttime (108 km) observations, which will be discussed in Sect. 4. The altitude registration of the tangent point for the temperature profiles is referenced to the middle of each row. Sample tangent altitude ground tracks for both MIGHTI-A and MIGHTI-B during one day of observations are shown in Fig. 4.

During the daytime portion of each orbit, the MIGHTI aperture is partially closed so that only approximately 15% of the light enters the pupil and the bright A-band limb emission, which can be several megaRayleighs at 90 km (Skinner and Hays 1985; Christensen et al. 2012; Yee et al. 2012), does not saturate the sensors. This also facilitates the rejection of bright signal from the lower atmosphere outside the field-of-view. The daytime images are taken at a cadence of 30 s, whereas at nighttime, when the emission rates are much weaker (e.g. Liu 2006), the aperture is completely open and the images are taken at a cadence of 60 s. The geolocation of the images at the tangent point for the temperature profiles is referenced to the middle of each integration time interval.

The required ICON  $1\sigma$  pointing accuracy is estimated to be  $\pm 0.37$  km vertically at the tangent point (Immel et al. 2018) and on-orbit operations indicate that ICON does better than this. The vertical sampling of each row varies from 3.1 km at 90 km to 2.9 km at 140 km for the retrieval of a temperature profile. Figure 5 shows the vertical resolution of the MIGHTI temperature profile retrieval, obtained from convolving the laboratory-measured point spread function with a boxcar function representing the 3 km spatial sampling of the MIGHTI sensors (pixel binning) on the limb. The nighttime function is broader due to the decreased imaging quality at night when the aperture is fully open. The results in Fig. 5 can be used, for example, to compare MIGHTI temperature profiles with profiles from other instruments or models at higher vertical resolution. Note that the design and focus of the MIGHTI optics was optimized for resolving the sinusoidal interference fringes in the wind

**Fig. 5** Averaging kernel for MIGHTI-A and MIGHTI-B, representing how much of the atmosphere is sampled at a tangent altitude for day (black) and night (red) for a single detector row. The full-width at half-maximum (FWHM) is indicated for each in the bottom right



channels (Harlander et al. 2017). As a result, the infrared channels have coarser vertical resolution, especially in night mode when the aperture is fully open.

The instantaneous horizontal distance sampled by one IR signal channel at the tangent point is 19.5 km. This is small compared to the horizontal smearing along the line of sight due to the 3 km vertical sampling of the instrument (Fig. 5), which is about 400 km at the minimum ray height as discussed in Sect. 4.1. There is also horizontal smearing along the orbital path of the spacecraft, which is about 190 km for a daytime exposure and 380 km for a nighttime exposure. Thus, one image of MIGHTI data has a vertical resolution of about 3 km and a horizontal resolution of about 200 km  $\times$  400 km during the day and about 400 km  $\times$  400 km at night.

ICON operates in normal science mode during the majority of the mission, where its remote sensing instruments are observing to the northward side of the orbit track in a “local vertical local horizontal” (LVLH) attitude. Another mode, reverse LVLH (rLVLH), consists of the remote sensing instruments observing southward, so the latitudinal coverage is roughly 42° S to 12° N instead of 12° S to 42° N. As of the time of writing, two periods of rLVLH have been performed: one during June 14–27, 2021 and one during April 10–14, 2022. The ICON orbit is such that tangent point locations can be sampled at all LT in one precession cycle, enabling the analysis of atmospheric processes that are diurnally driven. At the latitude extremes near 12° S and 42° N, full diurnal coverage (one precession cycle) is achieved in 48 days. However, for observations near the equator, both nodes of the orbit can be used and less than a full precession cycle is sufficient (Immel et al. 2018).

Various calibrations, maneuvers, and outages occur which cause gaps in the temperature data. These include conjugate maneuvers, calibration maneuvers for ICON’s ultraviolet instruments, and star tracker anomalies that caused the observatory to briefly enter safe mode. Other situations can occur that degrade the quality of the data to the point where it is unusable (*e.g.*, when the moon or sun is very close to the field-of-view, or when the spacecraft is experiencing increased radiation in the South Atlantic Anomaly). In these cases, the data have been either masked with fill values or completely removed from the data pipeline.

### 3 The MIGHTI Infrared Observations

#### 3.1 Raw Limb Images

MIGHTI began routine limb imaging on 6 December 2019 and has been operating nearly continuously since then. Before being passed to the temperature retrieval routines, the in-

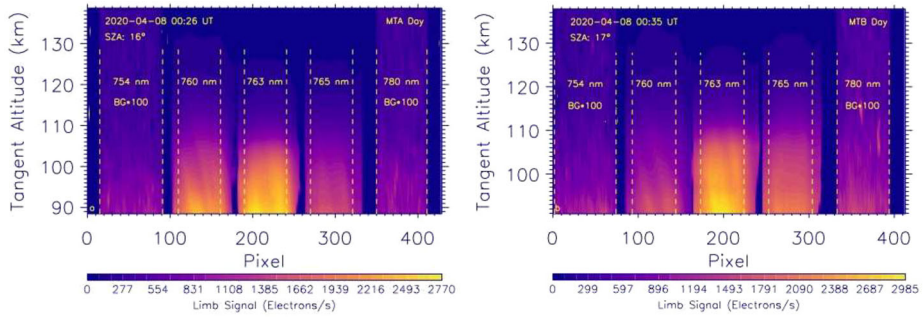


**Fig. 6** (a) Sample of an on-orbit MIGHTI-A daytime image at the indicated UT and solar zenith angle (SZA). The data shown are not flat fielded over pixels or over tangent altitude so that variations over the image include variations in the relative responsivity specific to each detector. The channel boundaries used are indicated by the vertical white dashed lines. The center wavelengths for each channel are indicated. The signals for the two background (BG) channels at 754.2 and 780.3 nm are multiplied by 100 to bring out the structure observed. (b) Same as Fig. 6a except a sample of a MIGHTI-B daytime image. The image is taken nine minutes after the MIGHTI-A image in Fig. 6a so that nearly the same volume of air is observed at the tangent altitude

frared images of the O<sub>2</sub> A-band are corrected for dark current, detector read-out bias, hot pixels, cosmic ray event spikes, and signatures of stars in the field-of-view. The images are converted from counts to electrons/second by accounting for the image integration time and the camera gain. Examples of MIGHTI-A and MIGHTI-B daytime images are shown in Figs. 6a and 6b. Note that the signal in the background channels in the first and last image has been multiplied by 100 to bring out the observed structure. It is notable that the background signal is therefore over 100 times less than what is recorded in the signal channels, indicating that any off-axis stray light is effectively suppressed in the MIGHTI infrared observations.

The images in Fig. 6 are not flat field corrected and therefore include variations of instrument responsivity and spectral passband across each channel that are quantified with pre-flight laboratory measurements (Fig. 2). For each row in Figs. 6a and 6b, the signal observed by the pixels within each channel is summed and multiplied by the integration time to obtain the total signal (in electrons) that is used in the temperature retrieval. The statistical uncertainty, or shot noise level in each signal channel is determined by the square root of the total number of free electrons created in the detector pixels, based on standard counting statistics.

Figures 7a and 7b show examples of MIGHTI-A and MIGHTI-B nighttime images, where the signal in the background channels is again multiplied by 100. As with the daytime images the background is small compared to the signal, providing evidence that any contaminating light in the signal channels is also small at nighttime. Note that the nighttime A-band emission shows a peak near 93 km, as expected (Greer et al. 1981; Liu 2006). Also note in Fig. 7 that there is additional emission in the 780 nm background channel for both MIGHTI-A and MIGHTI-B. This is likely due to OH(9,4) Meinel emission (Osterbrock et al. 1996), which peaks at night and will be discussed further in Sect. 4.1 in the context of the temperature retrieval.

### 3.2 Responsivity Modifications Using the Rayleigh Background

The version of the MIGHTI temperature product described herein and publicly available at the time of this writing is “v05”. Earlier versions of the data used laboratory measured



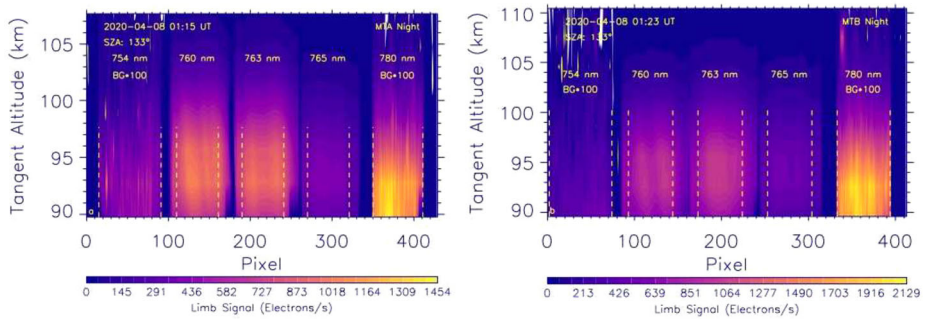


**Fig. 7** (a) Similar to Fig. 6a except a sample of an on-orbit MIGHTI-A nighttime image at the indicated UT and SZA. Note as with Fig. 6a the background channels at 754 nm and 780 nm have been multiplied by 100 to bring out structure. The enhancement in the 780 nm channel is likely due to the OH(9,4) Meinel band, which is primarily produced at night (see text). (b) Similar to Fig. 6b except a sample of a MIGHTI-B nighttime image

responsivity and passband wavelengths for each of the three signal channels and the two background channels. Although these earlier versions provided temperature profiles from MIGHTI-A, most of the MIGHTI-B data, including all of the MIGHTI-B nighttime data, was not released because it did not provide a solution that was consistent with MIGHTI-A. Even for the MIGHTI-A data, earlier versions only used two of the three available signal channels for the temperature retrievals, and for these earlier versions a single common wavelength shift to all channels at all tangent altitudes needed to be introduced to yield temperatures that were consistent with previously published, empirical climatologies. The lack of self-consistency within the MIGHTI dataset when analyzed using the pre-flight calibration data indicated that the responsivity and/or the channel wavelengths had changed. The responsivity of the MIGHTI channels may have changed during the more than three years long time period between the pre-flight calibration (June 2016) and launch (October 2019). Furthermore, a re-assessment of the channel center wavelengths that were available from pre-flight laboratory measurements showed that they were not of sufficient accuracy to be used as an absolute standard.

Although it was evident early on that modifications to the laboratory measured flat field calibrations were required for the on-orbit data, a persistent ambiguity results from the fact that a modification in a channel passband is correlated with a modification in a filter transmittance (channel responsivity). Given that there are two sensors, two modes of operation (day and night), and three different signal channels, a clear path to a self-consistent solution for all of the MIGHTI infrared observations was not obvious. To solve this problem, we looked for infrared light sources on-orbit.

One source of on-orbit background light is the broad band, bright, and well understood Rayleigh scattered solar background. The advantage of a broad band source in the context of the MIGHTI flat fields is that small variations in channel wavelengths, crucial in the temperature retrieval using the spectrally structured A-band, are much less important. Although any observations of Rayleigh scattered light would be mixed with A-band observations in the signal channels, the two background channels can serve to calibrate the relative spectral variation using the well-known spectral shape of Rayleigh scattered light in the daytime. A modification of the signal channel responsivities can be made by assuming a linear variation over the pixels corresponding to the passbands shown in Figs. 6 and 7. Such a linear responsivity change would be consistent with, *e.g.* a linear change in filter transmittance due to a

contamination event, or a linear illumination gradient in the pre-launch calibration measurements. Once the relative responsivities are re-calibrated, channel center wavelengths can be modified so that the three signal channels yield a self-consistent temperature profile between channels and the two MIGHTI sensors.

The modifications made to the responsivity and the channel center wavelengths based on these on-orbit measurements are described below in three sections. The first section describes the *daytime* responsivity modifications based on observations of Rayleigh scattered sunlight in the background channels obtained early in the mission. The second section describes the *nighttime* responsivity modifications based on special daytime operations allowing for Rayleigh scattered sunlight in the background channels with the MIGHTI aperture fully open in a “night” configuration. The third section describes the channel center wavelength modifications that enable a self-consistent solution for all three signal channels of MIGHTI-A and MIGHTI-B.

### 3.2.1 Responsivity Modifications: Daytime Mode

Our on-orbit modification of the pre-launch responsivity measurements is informed by the observed ratio of Rayleigh scattered light in the MIGHTI background channels compared to the expected ratio. Using the OSIRIS instrument on the Odin satellite, earlier limb observations at these wavelengths around the A-band by Llewellyn et al. (2004) found a limb radiance ratio of about 1.3 for 754.2 nm/780.3 nm near 60 km tangent altitude. In the near IR near 60 km OSIRIS limb observations are affected by off-axis stray light, which may affect this value (Sheese et al. 2010). Nonetheless, this ratio is consistent with the Moderate spectral resolution atmospheric Transmittance algorithm and computer model (MODTRAN) calculations by Llewellyn et al. of limb radiance ratios for the same wavelengths up to 90 km tangent altitude. The ratio of single scattered Rayleigh scattered light is that of the incoming solar irradiance, modified by the wavelength dependence of Rayleigh scattering. From the solar irradiances reported by Thuillier et al. (2003), the solar irradiance ratio for 754 nm/780 nm is 1.097. Applying an expected Rayleigh scattering wavelength dependence of  $1/\lambda^4$  we calculate an expected ratio of 1.257, which is within about 3% of the Llewellyn et al. results from both OSIRIS and MODTRAN. We use this expected value of 1.257 to inform our observations of the ratio of Rayleigh scattered sunlight in the MIGHTI background channels at these same wavelengths.

On 2 November 2019 ICON was in early mission operations, during which the MIGHTI field of view was oriented such that the bottom row of the imaging sensors was observing a tangent altitude of 73–77 km rather than the operational tangent altitude of 90 km. Although a correction to the pointing was made before normal operations started on 6 December, these early operations allowed for the detection of bright Rayleigh scattered sunlight in both MIGHTI infrared background channels of both sensors during the daytime portion of each orbit. The raw limb images obtained during these early mission operations were dark subtracted, gain corrected and divided by the exposure time. This is the same procedure used in normal operations to bring the infrared images to Level 1 (L1) and it results in signal levels for each pixel in the infrared channels in units of electrons/second. Figures 8a and 8b show the background limb signal from the daytime images for MIGHTI-A and MIGHTI-B, respectively on 2 November 2019. Here we limit our analysis to solar zenith angles less than  $70^\circ$  to avoid effects near the terminator, where a rapidly changing solar zenith angle along the line of sight could influence the channel ratios. The profile for each image as well as the average is shown for both the 754.2 nm background channel and the 780.3 nm background channel. It can immediately be seen that the ratio between them changes with altitude and

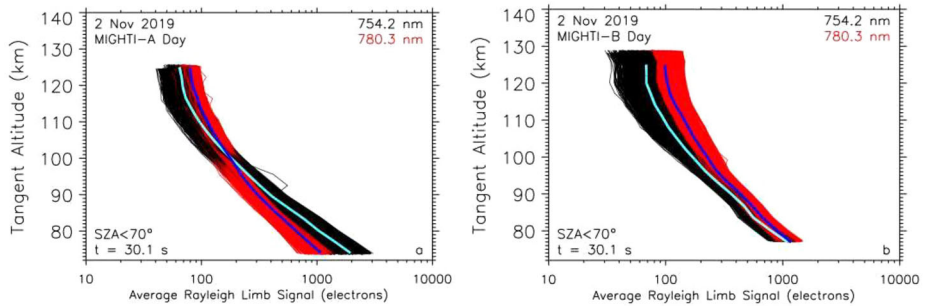


**Fig. 8** (a) MIGHTI-A images showing the Rayleigh scattered limb signal in the two background channels at 754.2 nm and 780.3 nm on 2 November 2019. The images are taken during the day with the bottom of the sensors at 73 km (MIGHTI-A) or 77 km (MIGHTI-B). The data are selected to avoid the terminator ( $<70^\circ$  SZA) and the integration time ( $t$ ) for each image is shown in the bottom left. The average of all the images is overplotted in dark blue (780.3 nm) and light blue (754.2 nm). (b) Same as Fig. 8a but for MIGHTI-B

that the limb signal at 754.2 nm is not always larger than at 780.3 nm. This evidence supports our earlier conclusion that the pre-launch calibrations need to be modified.

We note here that the observed signal in Fig. 8 approaches a constant value near the top of the images ( $\sim 110$  km), suggesting that another contribution to the signal other than Rayleigh scattering may be dominating the observations there (*e.g.* stray light within the instrument). We do not subtract any background from the profiles shown in Fig. 8, which could affect our analysis near the top of the images. However, our v05 temperature retrievals do not report results for the top  $\sim 10$  km of our images as we will show in Sect. 4, so that the departure from the expected behavior is largely avoided when the bottom of the field of view is at 90 km tangent altitude, as is typical. With this in mind, we proceed with our daytime responsivity modifications.

Next, the Rayleigh scattering observations in the background channels shown in Fig. 8 are analyzed based how their signal ratio compares to what is expected. Figures 9a and 9b show the ratio of the signal in the two background channels over all altitudes observed for MIGHTI-A and MIGHTI-B, respectively. In Fig. 9 we have removed profiles in Figs. 8a and 8b that are outliers and could bias the result, where this removal of profiles is based on the average and the scatter about the mean. Also shown in Fig. 9 is the ratio of the pre-launch responsivities as measured in the laboratory as well as the expected ratio observed, which is found by multiplying the ratio of responsivities by the Rayleigh scattering ratio calculated above. Although there is reasonable agreement at the very bottom rows for MIGHTI-A, the differences become larger at higher altitudes so that the observed ratio is about a factor of two lower than expected at the top. For MIGHTI-B the observed ratio is about a factor of two lower than expected at all altitudes.

Using the ratios in Fig. 9, Figs. 10a and 10b show how the responsivity for each of the five channels for MIGHTI-A and MIGHTI-B is changed so that they are consistent with the Rayleigh scattering ratio measured on-orbit. We are only concerned with relative changes across the five channels so we reference the changes to the background channel at 780.3 nm. In this calculation we assume that the variation between the two background channels is linear with pixel location on the sensor (see Figs. 6 and 7) to calculate the correction in the signal channels between the two background channels. For comparison, we have added results from another day of data when the MIGHTI line-of-sight was pitched low on 29 October 2019 and the results are very similar to 2 November 2019. The approach we use to retrieve temperatures is to model the emergent limb signal given our best understanding

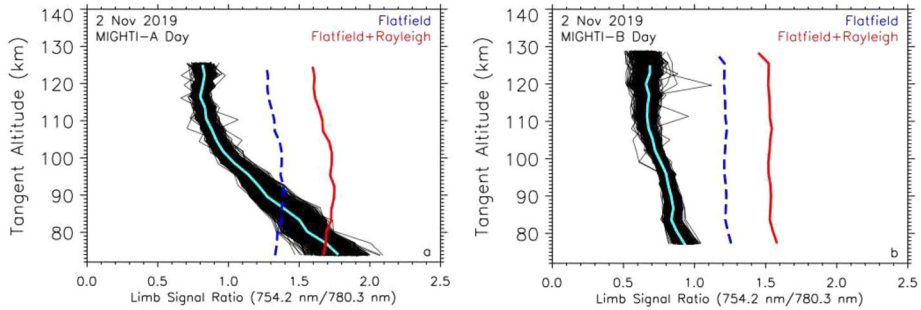


**Fig. 9** (a) Ratio of the background signals shown for MIGHTI-A in Fig. 8a. The average ratios are overlotted in light blue. The ratio of the mean responsivities measured in the laboratory prior to launch is shown in dashed dark blue and these values are multiplied by the calculated Rayleigh scattering ratio (1.257) and shown in solid red. The red curve therefore represents the expected ratio of Rayleigh scattered light observed by MIGHTI-A, whereas the light blue curve indicates the average ratio observed on-orbit. (b) Same as Fig. 9a but for MIGHTI-B

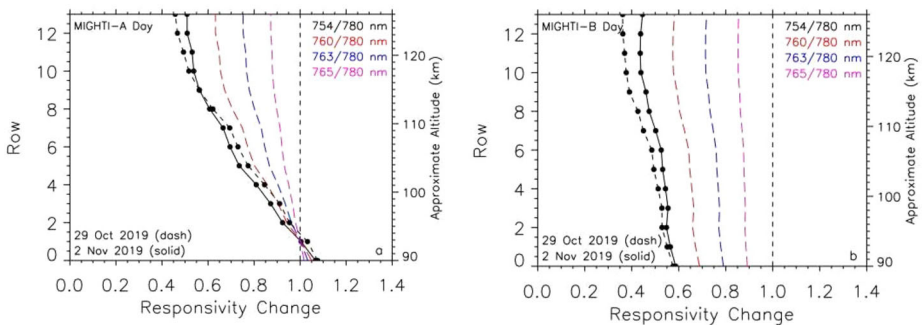


**Fig. 10** (a) Calculated responsivity change applied to those measured pre-flight for MIGHTI-A daytime conditions, using the averaged results from Fig. 9a on 2 November 2019 and linearly interpolating over pixels to the three signal channels at 760 nm, 763 nm, and 765 nm. The relative changes are referenced to the 780 nm channel. They are plotted vs. sensor row on the left-hand axis and approximate tangent altitude for typical MIGHTI operations on the right-hand axis, where the bottom row is at 90 km tangent altitude. These scale factors are used to modify the pre-flight measured responsivities of each channel. For comparison, results from another day of observations for the two background channels on 29 October 2019 are shown as the black dashed line. (b) Same as Fig. 10a except for MIGHTI-B daytime conditions

of the instrument, including the responsivity modifications shown in Fig. 10. To that end, we multiply the pre-flight measured responsivities in daytime operating conditions with the scale factors shown in Figs. 10a and 10b.

### 3.2.2 Responsivity Modifications: Nighttime Mode

Quantifying the response of MIGHTI to Rayleigh scattered sunlight under nighttime operating conditions required special operations. Because the aperture is typically completely open for nighttime operations to observe the weaker A-band emission then, the sensors would saturate if operated in nominal nighttime operations during the day. To avoid this problem, two orbits of MIGHTI-A and MIGHTI-B observations were obtained for which the aperture was fully open during the day, but the integration time was reduced from the nominal 60 s to 2 s, so that the detectors would not saturate. The observation of Rayleigh scattered light with a

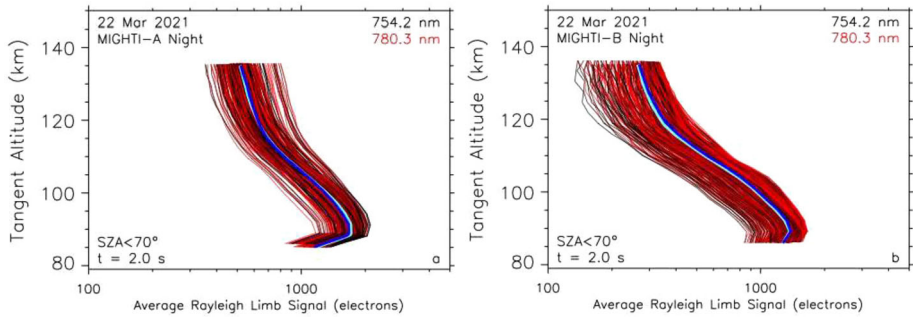


**Fig. 11** (a) MIGHTI-A images showing the Rayleigh scattered limb signal at 754.2 nm and 780.3 nm for the two orbits of daytime data collected using the nighttime aperture setting on 22 March 2021. The integration time for these observations was reduced to 2 s from the nominal 60 s for nighttime operations to avoid saturation effects. Results from individual images are shown and the average of all of them is overplotted in dark blue (780.3 nm) and light blue (754.2 nm). The observations were made with the MIGHTI aperture completely open (“Night” configuration) and the integration time reduced to 2 s from 60 s to avoid sensor saturation. (b) Same as Fig. 11a but for MIGHTI-B

nighttime aperture setting during the day also avoids any possible contamination by the OH Meinel bands in this spectral region (see Fig. 7), because the Meinel band emission is weak during the day compared to the A-Band emission (Yee et al. 1997; Marsh et al. 2006). These data were obtained on 22 March 2021 and processed to L1 as described in Sect. 3.2.1.

Figures 11a and 11b show the average limb signal obtained from the MIGHTI-A and MIGHTI-B sensors in the background channels while observing the atmosphere during the daytime with the instrument operating in nighttime mode. We note here that even though the MIGHTI integration time was only 2 s, the cadence of the images acquired over the two orbits is still 30 s, which is nominal for daytime operations. The limb signal decreases exponentially with increasing altitude except at the bottom and at the top of the images. A change in slope is seen at about 110 km, which was similarly observed during the observations of Rayleigh scattered light in the MIGHTI daytime configuration as discussed in Sect. 3.2.1. Although this suggests that Rayleigh scattering is not dominating the signal in this region, our nighttime temperature profiles are not reported above 108 km so this behavior is again avoided in the reported temperatures. Below 90 km the signal has the opposite behavior than expected from Rayleigh scattering likely due to vignetting at the lowest altitudes near the edge of the sensor.

Figures 12a and 12b show profiles of the MIGHTI signal ratios for the average background limb signals shown in Figs. 11a and 11b. These profiles are nearly constant with altitude for both sensors, despite the fact that the raw signal profiles exhibit an exponential decrease with altitude in Fig. 11. As for the daytime Rayleigh scattered observations in Fig. 9, these ratios are significantly smaller than expected from the pre-launch calibration.

Using the ratios in Fig. 12, Fig. 13 shows how the responsivity of each of the MIGHTI channels is changed so that they are consistent with the Rayleigh scattering ratio observed on-orbit. The results are again referenced to the 780.3 nm background channel and again interpolated linearly based on the location of each signal channel in pixel space, as was done in Fig. 10 for the daytime configuration.

### 3.2.3 Wavelength Modifications

Once the responsivity modifications are implemented for both sensors and for both modes of operation, we focus on the calibration of the signal channel wavelengths. These were

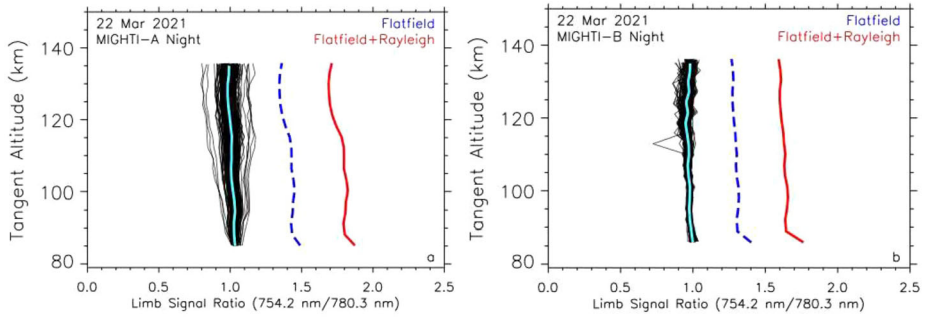


**Fig. 12** (a) Ratio of the signal shown for MIGHTI-A observations in “Night” configuration from Fig. 11a, where the observations are made during the day with the indicated shorter integration time. The different curves are analogous to what is shown in Fig. 9a, where the red curve indicates the expected ratio and the light blue curve shows the average observed ratio. (b) Same as Fig. 12a but for MIGHTI-B in “Night” configuration

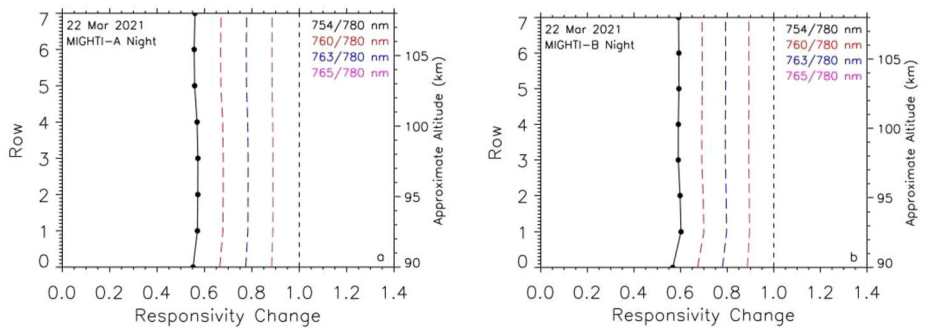


**Fig. 13** (a) Calculated responsivity change to the pre-flight measured values for MIGHTI-A “Night” configuration, using the results from Fig. 12a at each row (tangent altitude) sampled by the sensor for typical viewing conditions, where the bottom row is at 90 km tangent altitude. The changes to the three signal channels at 760 nm, 763 nm, and 765 nm are linearly interpolated over pixels between the background channels. The relative changes are referenced to the 780 nm channel. (b) Same as Fig. 10a except for MIGHTI-B “Night” configuration

also measured during pre-flight calibration measurements. Unlike the Rayleigh scattering observations discussed above, the A-band temperature retrieval is extremely sensitive to the wavelength registration of the signal channels, due to the discrete lines populating the A-band emission spectrum (Fig. 1). The modifications to the three signal channel wavelengths were made so that all three channels in MIGHTI-A and, independently, MIGHTI-B yielded a self-consistent solution.

The approach to these wavelength adjustments is as follows. First, we employed a common wavelength shift to all signal channels and all rows by the same amount. Second, we further modified the wavelengths as a function of row (altitude) for all three signal channels by the same amount for each row on each sensor so that they yielded as close to a consistent solution for the limb signal as possible. Third, we modified the wavelengths for all rows by the same amount but in opposite directions for the first (760 nm) and third (765 nm) signal channels to optimize the agreement of the three signal channels. Throughout this process, we ensured that the temperature at the bottom of the profiles near 90 km was very close (within 10 K) to that from the Mass Spectrometer Incoherent Scatter radar empirical model

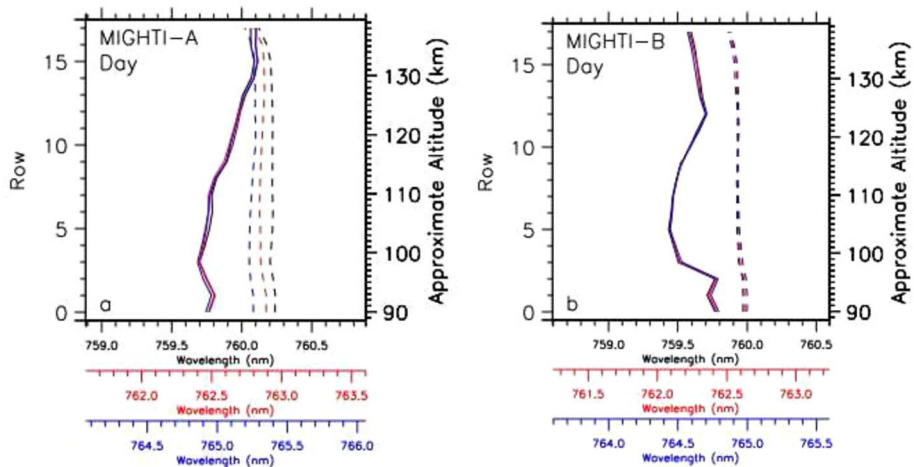


**Fig. 14** (a) Center wavelengths measured pre-flight (dashed) and adopted for the MIGHTI-A daytime channels in v05 (solid). Each signal channel is shown at 760 nm (black), 763 nm (red), and 765 nm (blue). The range on each x-axis is 2 nm, which approximately represents the full-width at half-maximum of each filter passband (see Fig. 2). The wavelength modifications shown for v05 allow for a self-consistent solution between all three signal channels. (b) Same as Fig. 14a except for the MIGHTI-B daytime channels

(MSIS 2.0) because of the widespread agreement between satellite and ground-based temperature observations at this lowest altitude observed by the MIGHTI sensors (Emmert et al. 2020). A more quantitative comparison against existing datasets is presented in Sect. 5.

The results of the above modifications, along with the pre-flight wavelength calibrations, are shown in Fig. 14a for MIGHTI-A day and 14b for MIGHTI-B day. They are typically less than 0.5 nm at all rows (altitudes). To show the improvement of forward-modeled solutions to the data, we compute a forward solution for each channel and show the ratio of data/model for all three channels in Fig. 15a for MIGHTI-A day and Fig. 15b for MIGHTI-B day. These are all very close to unity at all altitudes, indicating that all channel signals are consistent with the same solution for temperature. Also shown in Fig. 15 are the solutions using the pre-flight flatfields with no modifications for comparison. Details on the forward model are discussed in the next section.

Figures 16a and 16b show the wavelength modifications made to the MIGHTI-A nighttime and MIGHTI-B nighttime signal channels. Pre-flight derived channel center wavelengths are also shown. Figures 17a and 17b show the comparison of data and retrieved forward solutions both with and without the flat field adjustments, analogous to Figs. 15a and 15b in the daytime. Again, the improvement to the solution for MIGHTI-A nighttime is significant in Fig. 17a. We note here that a self-consistent solution of the three signal channels for MIGHTI-B night could not be found so we modified the wavelengths of those channels so that the retrieved temperatures at night were consistent with MIGHTI-A at night. Therefore, although the three MIGHTI-B night channels agree well below 95 km in Fig. 17b, above this altitude the forward solutions diverge. However, the retrieved temperatures and their variability are consistent with MIGHTI-A night, as we will show in the next section.

The channel center wavelengths shown in Figs. 14 and 16 are determined for typical LVLH operations when MIGHTI-A views  $45^\circ$  in azimuth from the satellite ram direction and MIGHTI-B views  $45^\circ$  in azimuth from the wake direction. As discussed in Sect. 2.2, ICON is occasionally yawed so that the lines of sight for MIGHTI-A and MIGHTI-B are

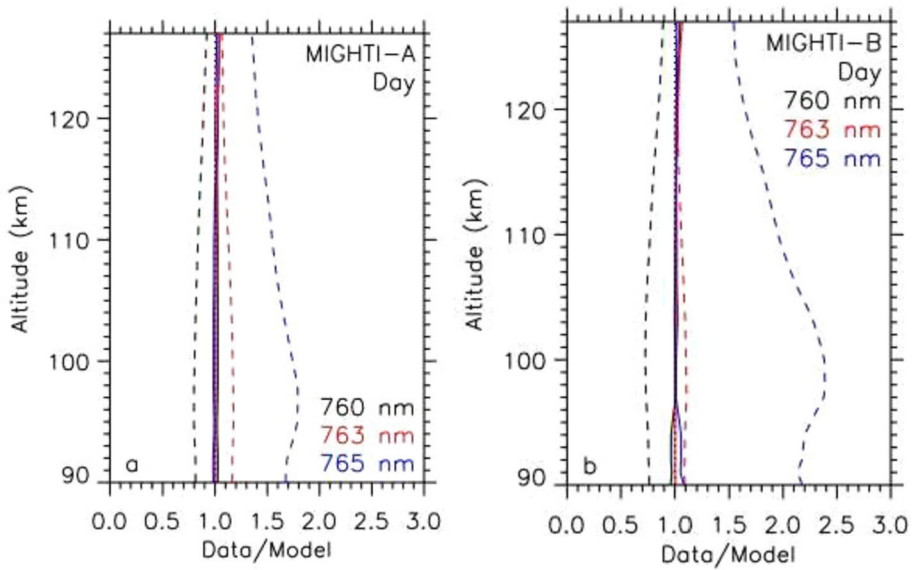


**Fig. 15** (a) Ratio of the limb data to forward modeled signal for MIGHTI-A daytime observations using the preflight responsivities and channel center wavelengths are shown as the dashed lines for the three signal channels. An optimal fit to the data at 760 nm (black), 763 nm (red), and 765 nm (blue) would show Data/Model=1.0 at all altitudes. Following the modifications to responsivities and wavelengths, the ratio of the observed signal and retrieved signal is shown as the solid lines. The data represent the average over one orbit of observations on 8 April 2020. (b) Same as Fig. 15a except for MIGHTI-B daytime data

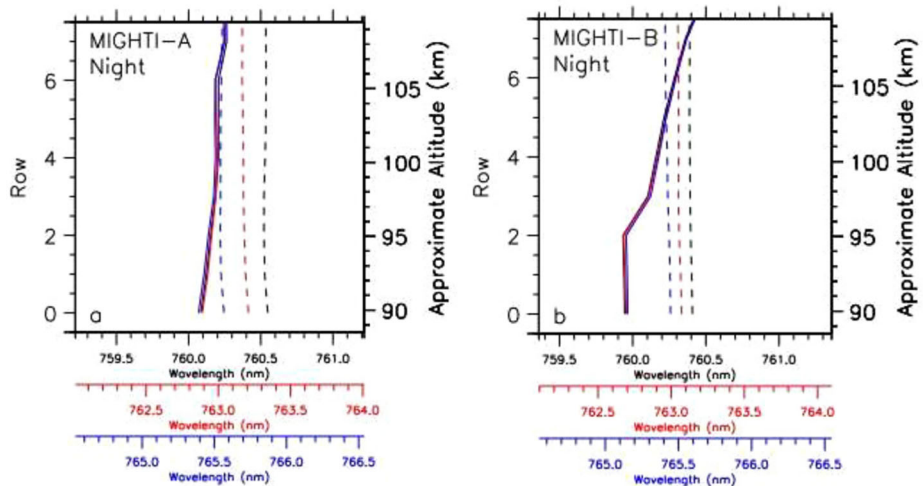


**Fig. 16** (a) Same as Fig. 14a except channel center wavelengths for the MIGHTI-A nighttime. (b) Same as Fig. 15a except for the MIGHTI-B nighttime

directed southward instead of northward. In this rLVLH configuration the view directions of MIGHTI-A and MIGHTI-B are reversed with respect to the satellite ram direction. Under these conditions, we find that a small correction needs to be made to the MIGHTI-A



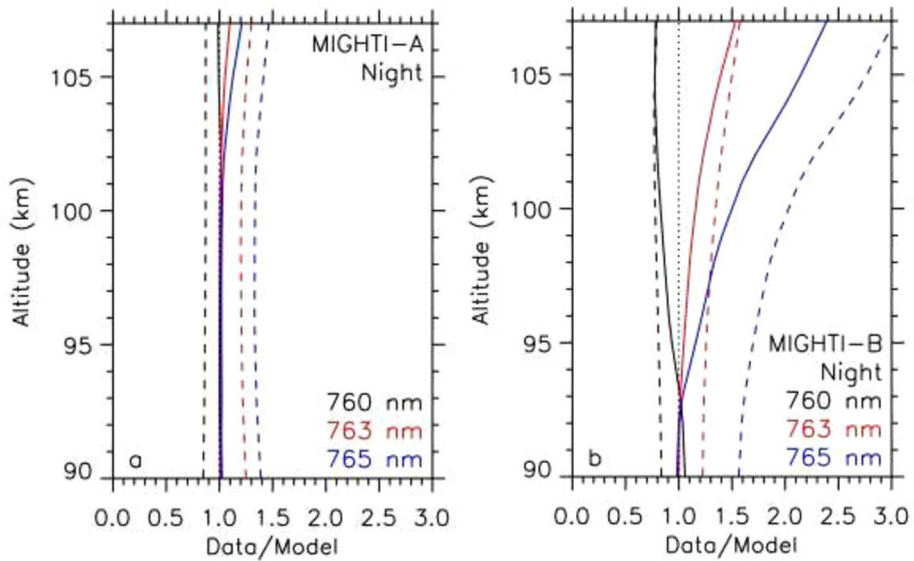


**Fig. 17** (a) Same as Fig. 15a except for MIGHTI-A night. (b) Same as Fig. 15b except for MIGHTI-B night. A self-consistent solution with MIGHTI-B night was not possible so the wavelengths for the signal channels were modified so that the MIGHTI-B nighttime temperatures agreed to the MIGHTI-A nighttime temperature on average

and MIGHTI-B channel wavelengths and in opposite directions to account for the different Doppler shift caused by the projection of the satellite velocity onto the view directions. This was verified during rLVLH operations in June 2021, producing much better agreement between MIGHTI-A and MIGHTI-B retrieved temperatures.

### 3.2.4 Other Possible Contaminating Features

Limb observations by the Remote Atmospheric and Ionospheric Detection System (RAIDS) by Christensen et al. (2012) revealed no evidence of contaminating features within the passbands of the MIGHTI infrared channels shown in Fig. 2. Indeed, the MIGHTI data shown in Figs. 6 and 7 reveal no significant evidence of contaminants within the signal or background channels. However, small contributions that are masked by the bright A-band signal could in principle affect the temperature retrieval. Slanger et al. (2017) suggested that the  $N_2$  first positive group (1PG)  $B^3\Pi(3)-A^3\Sigma(1)$  band near 763 nm could contribute to the determination of temperature using the A-band in this spectral region. In a pre-launch study using the MIGHTI specifications, Stevens et al. (2018) estimated that this band could affect MIGHTI retrieved temperatures by up to 10 K at 140 km if all of the  $N_2$  1PG (3,1) band emission were in the middle signal channel at 763 nm, with no other 1PG emission contributing. The estimated effect on retrieved temperature at 90 km in this extreme case was less than 2 K. Here we better quantify this effect with a band model and expected dayglow radiances throughout the A-band spectral region using our improved flat fields.

For this analysis we use the Atmospheric Ultraviolet Radiance Integrated Code (AURIC; Strickland et al. 1999) to explicitly quantify the distribution of  $N_2$  1PG emission within all the MIGHTI channels and at all observed altitudes. The excitation of  $N_2$  1PG is calculated from photoelectron impact and Fig. 18 shows the results for limb emission at a tangent

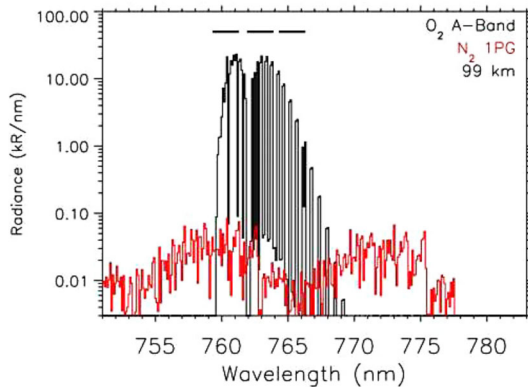


**Fig. 18** Calculated limb emission of the  $O_2$  A-band and the  $N_2$  1PG system looking toward a tangent altitude of 99 km. The total A Band radiance is 4.4 MR, consistent with the observations of Skinner and Hays (1985) and is calculated using a temperature of 174 K. The  $N_2$  1PG (3,1) band is indicated by the emission from 755763 nm and the band from 767775 nm is the (2,0) band. The  $N_2$  1PG bands are calculated for the same conditions as the A-band. Both spectra are binned at 0.1 nm resolution. A-band emission in signal channels indicated at the top at 760, 763, and 765 nm is at least two orders of magnitude brighter than  $N_2$  1PG. MIGHTI background channels are at 754.2 nm and 780.1 nm, where  $N_2$  1PG radiances are weak

altitude of 99 km. Solar fluorescence is not included here but is not expected to be important since the transition terminates on the A state of  $N_2$  rather than the ground state. Figure 18 shows that  $N_2$  1PG emission appears in all signal channels at 760 nm, 763 nm, and 765 nm. As shown in the figure, this emission is small compared to the A-band limb emission at 99 km, which is several MegaRayleighs (Skinner and Hays 1985).  $N_2$  1PG emission in the MIGHTI background channels at 754.2 and 780.1 nm are located is even weaker.

By calculating the  $N_2$  1PG emission in each signal channel and distributing the A-band limb emission observed by Skinner and Hays into the three MIGHTI signal channels using an MSIS temperature profile (Emmert et al. 2020) consistent with the indicated conditions, we find a ratio of  $N_2$  1PG limb emission to A-band emission as a function of altitude. This  $N_2$  1PG contribution is less than 3% for all channels at and below 125 km. We reduced the emission in each of the channels by the estimated amount for each altitude and find that the  $N_2$  1PG system affects the retrieved MIGHTI temperatures by less than 1 K at all observed altitudes below 120 km. This effect is small because the  $N_2$  1PG system emission is distributed between all three channels so that the resulting change in the channel ratios is reduced.

We also used AURIC to determine the potential contribution from any other emission features within the MIGHTI channels shown in Fig. 18. We found a small amount of emission near 99 km due to  $N_2^+$  Meinel bands, but the amount was less than 1% of the value calculated for  $N_2$  1PG for the same altitude so that its effect on retrieved temperatures is negligible.

The emissions of the hydroxyl (OH) Meinel bands, which peak in the upper mesosphere at night near 88 km altitude (*e.g.* Liu and Shepherd 2006) are not included in these AURIC calculations. Some of the relatively weak (4,0) Meinel band is observed from the ground within the MIGHTI signal and background channels (Osterbrock et al. 1996). We calculated the OH Meinel spectrum at 200 K from HITRAN2016 (Gordon et al. 2017) and scaled the relative intensities of the  $v' = 4$  progression to the (4,2) band (Harrison and Vallance Jones 1957). By converting the overhead (4,0) radiance to a limb geometry and comparing

to the expected nighttime A-Band (0,0) nighttime limb emission, we found that the relative contribution is similar for all MIGHTI signal channels above 90 km and is consistently 1% or less, which is less than that determined from the N<sub>2</sub> IPG emission above and therefore does not significantly affect the temperature retrievals. The potential effects of the OH Meinel (9,4) band in the 780 nm background channel at night described in Sect. 3.1 is discussed more quantitatively in the next Section in the context of the temperature retrieval.

## 4 The MIGHTI Temperature Retrieval

Previous work by Stevens et al. (2018) used pre-flight specifications of MIGHTI and the known MLT emission rate profile of the A (0,0) band to show that simulated temperature retrievals were consistent with measurement requirements for the ICON mission (Immel et al. 2018). By contrast, in this Section we use the on-orbit modifications to the sensitivities and channel center wavelengths presented in Sect. 3 to describe the MIGHTI v05 operational temperature retrieval and show a sampling of the results obtained to date. One important advance compared to the pre-flight study of Stevens et al. is that we now treat observations from the MIGHTI-A and MIGHTI-B sensors separately.

### 4.1 The Forward Model

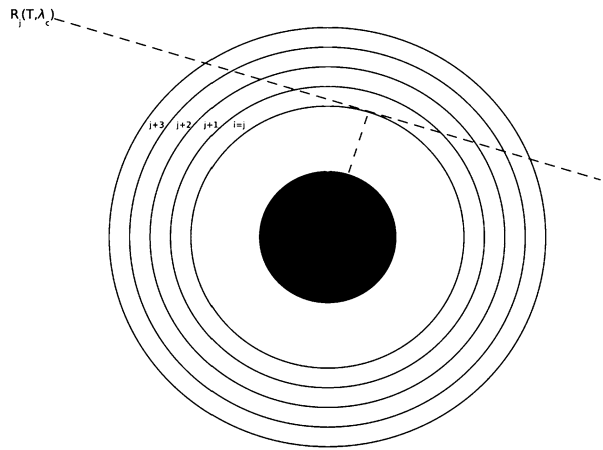
The approach to the operational retrieval is to find a temperature profile for each observed MIGHTI image (A or B, day or night) that is a least-squares best fit to the observed A-band limb signal in all three signal channels. The vibrational distribution of the O<sub>2</sub> <sup>1</sup>Σ molecules are in local thermodynamic equilibrium up to about 120 km in both daytime and nighttime (Yee et al. 2012; Slinger et al. 2003) so that the rotational distribution accurately represents the ambient neutral temperature at the observed tangent altitude of MIGHTI.

As illustrated schematically in Fig. 19, for each limb image MIGHTI simultaneously detects the emergent emission from tangent altitudes between about 90 km and 140 km. In order to retrieve the local temperature at a particular tangent altitude, contributions of the signal from all altitudes above the tangent altitude are quantified and removed. The discrete path integral that defines each tangent altitude as a layer is explicitly calculated from the top layer  $n$  to tangent layer  $j$  is given by

$$R_j(T, \lambda_c) = 2V [T_n(\lambda_c)] ds_{n,j} + 2 \sum_{i=n-1}^j V [T_i(\lambda_c)] ds_{i,j} \quad (1)$$

where  $R$  is the total signal along the line of sight at tangent layer  $j$ ,  $V$  is the volume emission rate at each layer along the line of sight,  $T_i$  is the temperature at each layer  $i$ ,  $\lambda_c$  is the signal channel wavelength, and  $ds_i$  is the path length at each layer along the line of sight through the atmosphere from the satellite to the tangent point. The factor of two is included in both terms on the right hand side of Eq. (1) to account for both the near and far field contributions along the line of sight, given that the emission is optically thin. The top layer  $n$  is treated differently than the other layers in Eq. (1) as discussed below. Figure 19 is not to scale but demonstrates that the 3 km vertical resolution of the observations translates into a much larger horizontal smearing along the line-of-sight, which is about 400 km for the MIGHTI temperature observations. We start from the top of each image and determine the signal and temperature for each layer below that sequentially, under the assumption of spherical symmetry along each line of sight as shown in Fig. 19.

**Fig. 19** Schematic representation of the observational geometry informing the temperature retrieval showing the line-of-sight through discrete, spherically symmetric layers and through a tangent layer  $j$ . The emergent limb signal observed by MIGHTI is given by  $R_j(T, \lambda_c)$  and represents contributions from tangent layer  $j$  and all layers above it



Special consideration must be given to the top layer observed (layer  $n$  in Eq. (1)), as it also contains information from all altitudes above it, which are not explicitly observed. This is particularly important during daytime operations when the emission has a large scale height and extends beyond the top layer that is observed by MIGHTI. For this top layer, we calculate an emission scale height for each signal channel separately and a Chapman function (Brasseur and Solomon 1986) to estimate this contribution, *i.e.*

$$ds_{n,n}(\lambda_c) = \sqrt{\frac{\pi R(z_n) H_n(\lambda_c)}{2}} \quad (2)$$

where  $H_n(\lambda_c)$  is the scale height at the top of the emission profile for each signal channel  $\lambda_c$  (760 nm, 763 nm, or 765 nm), and  $R(z_n)$  is the radial distance from the center of the earth at the top layer. The scale height is calculated for each channel from a fit to the signal at the top four tangent altitudes.

Another consideration is the contribution from the upper, unobserved layers when MIGHTI is looking below the highest tangent altitude in the field of view ( $ds_{n,j}$ ;  $n \neq j$ ). This contribution is smaller than the highest tangent altitude contribution ( $ds_{n,n}$ ). The calculation for these path lengths is done numerically using an MSIS temperature profile that extends to the exosphere and a simulated A-band volume emission rate (Stevens et al. 2018). We find that the relative weighting of the Chapman function is reduced by more than factor of 10 when looking below tangent altitudes of 110 km during the day.

The approximation for the effective path length of the top tangent layer described in Eq. (2) ( $ds_{n,n}$ ) assumes a constant scale height above the top layer, which is not necessarily a good assumption for the lower thermosphere. To estimate the uncertainty introduced by this assumption, we have considered two extreme cases of exospheric temperatures using the MSIS empirical model (Emmert et al. 2020). We ran a forward model of emission with a lower exospheric temperature and compared against a profile with a higher exospheric temperature. The differences at the tangent altitude are about 7 K at 125 km but 1 K or less at 110 km and below. This is included in the altitude dependent bias uncertainties reported for the MIGHTI temperature product. The above uncertainties are significantly mitigated in the operational temperature product because the daytime retrievals begin at the top layer near 140 km whereas the reported temperature profiles begin at the first layer below 127 km.

Figures 20a and 20b show sample daytime limb profiles for the three signal channels and their corresponding statistical uncertainties, as well as the background signal that has been

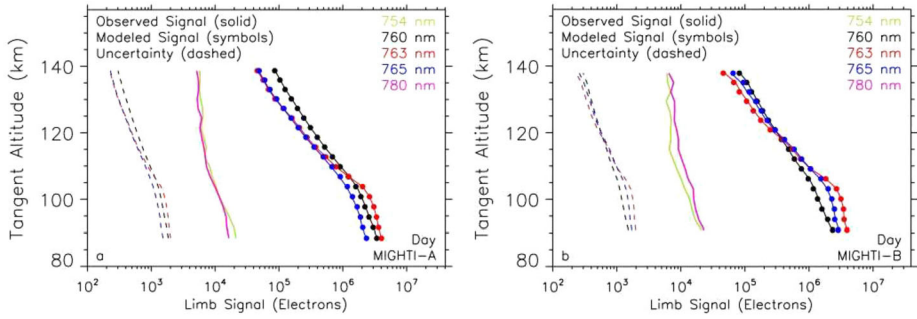


**Fig. 20** (a) Limb observations from the three MIGHTI-A signal channels during daytime from the same sample image as Fig. 6 on 8 April 2020 (solid lines). The wavelength of each of the signal channels is indicated by color in the upper right and background signals at 754 nm and 780 nm are also shown. The retrieved signals for the same image are shown as the closed circles, which are nearly identical to observations for each channel. Signal precision for each tangent altitude is shown with the dashed lines. (b) Same as Fig. 20a except for a MIGHTI-B daytime image on the same day

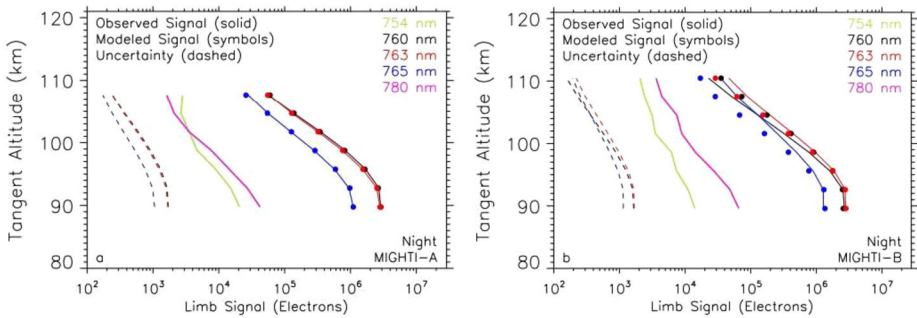


**Fig. 21** (a) Limb observations from the three MIGHTI-A signal channels during nighttime from same sample image as Fig. 7 on 8 April 2020 (solid lines) along with background signals at 754 and 780 nm. The retrieved signals are shown as the closed circles. Signal precision is shown with the dashed lines. (b) Same as Fig. 21a except for a MIGHTI-B nighttime image on the same day

subtracted. For each MIGHTI image, the limb signal is calculated for each channel and each tangent altitude according to Eq. (1) so that the forward solution matches the data best, using the least squares metric. This is done using an initial guess for temperature and iterations until an optimal fit is found for all signal channels using a Levenberg-Marquardt least-squares fitting procedure (Markwardt 2009) with no regularization. Examples of retrieval results from one MIGHTI-A and one MIGHTI-B daytime image are shown in Figs. 20a and 20b, respectively. The agreement between the model solution (closed circles) and the data (solid lines) is very good for each signal channel and each tangent altitude, which demonstrates that the signal from the three channels within each sensor represent a self-consistent solution.

Similar examples for a MIGHTI-A and MIGHTI-B nighttime images are shown in Figs. 21a and 21b, respectively. The agreement between the observed and retrieved signal is very good for MIGHTI-A nighttime. As discussed in Sect. 2, the agreement is not as good for MIGHTI-B nighttime at the upper tangent altitudes, but the retrieval nonetheless finds a best fit, using all three channels. As discussed in Sect. 3.1, the nighttime background channel at 780 nm is likely detecting some of the OH(9,4) Meinel band at the bottom of of

the profiles in Fig. 21 (Yee et al. 1997), but the emission is still very weak compared to the A-band emission in the signal channels. The contribution from the OH(9,4) band to the 780 nm background channel is minimized by the narrow filter (Fig. 2e) that only samples a small portion ( $<10\%$ ) of the OH(9,4) band and does not significantly affect the temperature ( $<1$  K) when comparing against a retrieval using only the 754 nm signal as a background.

There are some limitations to the approach discussed above. The A (0,0) band becomes optically thick in the upper mesosphere (Yee et al. 2012) and there is also on-orbit evidence that the responsivity and/or the channel center wavelengths at the bottom row of the sensors are not as well characterized as those rows above. These limitations become important below the lowest altitude required for the MIGHTI temperature retrieval (90 km; Englert et al. 2017) but we have nonetheless removed all retrieved temperatures below 88 km, in order to limit any such potential biases.

We begin all retrievals at the top layer observed, provided there is a signal that is bright enough to infer a temperature. However, due to the lower volume emission rates for the A (0,0) band at night, we have empirically determined that those retrieved profiles are unreliable above 108 km for MIGHTI-A and 106 km for MIGHTI-B due to insufficient signal, and we have removed these results from the v05 product. The lack of observations above 140 km during daytime affects the retrieval near the top as discussed and we have furthermore empirically determined that MIGHTI-A and MIGHTI-B temperatures are not self-consistent above 127 km so we have also removed these results from the v05 product.

In addition, and as discussed in Sect. 2.2, when MIGHTI transitions from nighttime operations (aperture 100% open) to daytime operations (aperture about 15% open), and vice versa, there are images that saturate the detectors due to brighter daytime A-band emission in the field of view. All images are tested for saturation and removed from processing and those near the terminator are particularly susceptible to this effect. These saturated images are removed from the data pipeline and not processed, leaving some short data gaps at this time of day.

MIGHTI images are also susceptible to enhanced particle precipitation within the South Atlantic Anomaly, as discussed in Sect. 2.2. Such an environment often compromises the temperature retrieval. In order to address this problem, we use a data driven, empirical approach to finding the contaminated images. We assemble the MIGHTI limb signals from each channel in  $3^\circ$  solar zenith angle bins for each day and test each image for outliers. If a measured signal is more than  $5\sigma$  above the mean within that bin in any of the channels, then that image is removed from processing. This removes any outliers, and the images removed are clustered near the South Atlantic Anomaly (see Fig. 4).

## 4.2 Retrieved Temperature Profiles

In this Section, we use the retrieval for an entire day of images from 8 April 2020 for both MIGHTI-A and MIGHTI-B and compare the temperature profiles to check for self-consistency in the two datasets. For this comparison, we separate daytime and nighttime data and we also only select data for which MIGHTI-B images are taken nine minutes after MIGHTI-A images to ensure that the two sensors are measuring nearly the same volume of air at the tangent altitude. With this constraint, Fig. 22a shows all MIGHTI-A and all MIGHTI-B daytime temperature profiles for 8 April. The daytime profiles in Fig. 22a are assembled without regard to latitude or LT because the emphasis of the figure is to compare concurrent results from the two sensors. Due to the large amount of variability in the temperature profiles, we have also overplotted the averages of each as dashed lines in Fig. 22a. For all temperature retrievals we remove profiles for which any tangent point temperature is

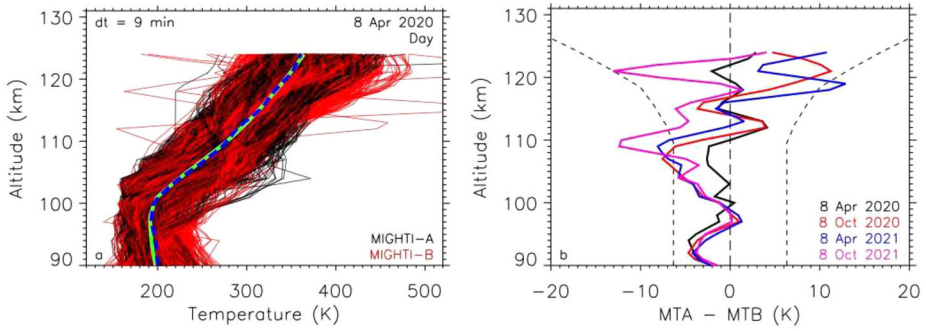


**Fig. 22** (a) A day of temperature profiles at all observed latitudes and daytime LT for MIGHTI-A (black) and MIGHTI-B (red). For all of these profiles MIGHTI-B is measuring nearly the same volume of air at the tangent point as MIGHTI-A but nine minutes later. Miss distances at the tangent point are less than 150 km. The average of these is shown as green for MIGHTI-A and blue dashed for MIGHTI-B. (b) The difference of the MIGHTI-A and MIGHTI-B averages (MTA-MTB) in Fig. 22a. Also overplotted are daily daytime differences from 3 other days, each 6 months apart. The estimated uncertainty (black dashed lines) is the addition of MIGHTI-A and MIGHTI-B bias uncertainties

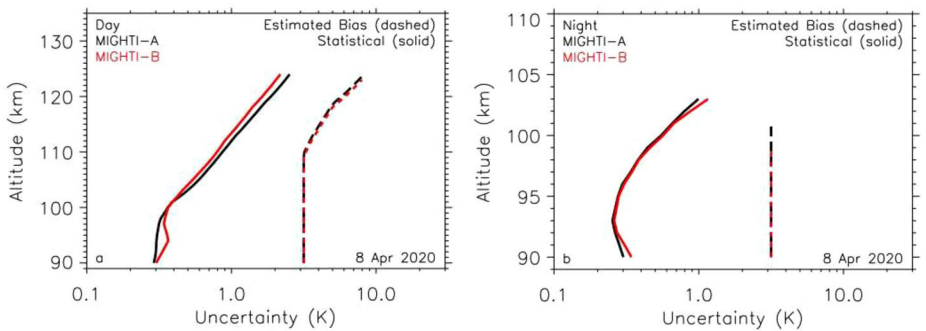


**Fig. 23** (a) Average statistical (solid) and estimated bias (dashed) uncertainties for daytime MIGHTI-A and MIGHTI-B observations. The estimated bias uncertainty is due to uncertainty in MIGHTI flat fields (all altitudes) as well as the uncertainty in the contributions from above the top layer of the retrievals (above ~110 km), which start near 140 km. The uncertainties are averaged over the indicated day. (b) Same as Fig. 23a except for nighttime observations

below 100 K or above 1000 K to avoid introducing outliers that could bias the averages. As stated in Sect. 2, MIGHTI tangent point latitudes nominally extend to 42° N so it does not sample the polar summer mesopause, where temperatures can sometimes approach 100 K.

We subtract the average MIGHTI-B daytime profile in Fig. 22a from the average MIGHTI-A profile and show the result in Fig. 22b. Also plotted are differences in the daily averages in six month increments starting from 8 April 2020 (8 October 2020, 8 April 2021, and 8 October 2021). Figure 22b demonstrates that the differences between the MIGHTI-A and MIGHTI-B average daytime temperature profiles show similar structure over a year. Indeed, it is these differences that help inform our estimation of the bias uncertainties, which are shown in Fig. 23a for MIGHTI-A and Fig. 23b for MIGHTI-B along with the average statistical uncertainty for each image. The MIGHTI-A and MIGHTI-B differences are less than 7 K from 90 to 105 km and very close to the combined estimated bias uncertainties of the two measurements, which are added and overplotted in Fig. 22b. At the lower altitudes

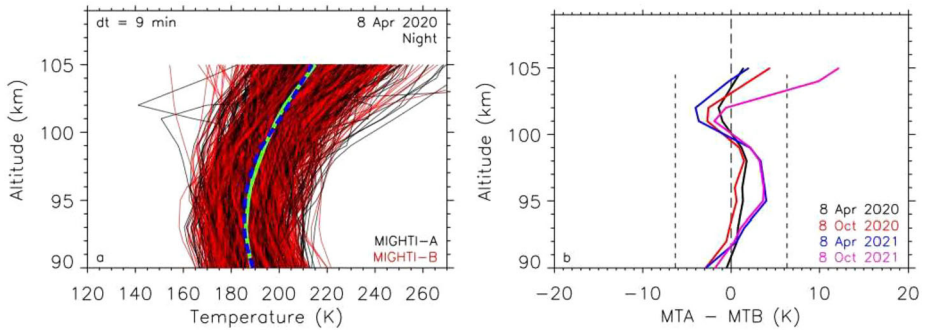


**Fig. 24** (a) Same as Fig. 22a except for nighttime conditions. The average of these is shown as green for MIGHTI-A and blue dashed for MIGHTI-B. (b) Same as Fig. 22b except for nighttime conditions

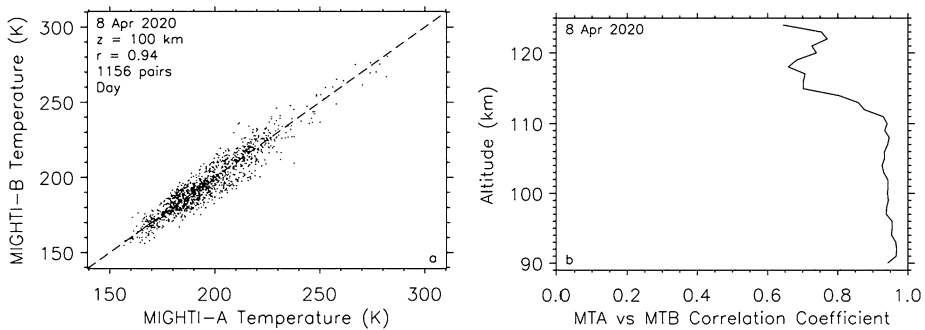


**Fig. 25** (a) MIGHTI-A and MIGHTI-B daytime temperatures from Fig. 22a interpolated to 100 km altitude and compared. They are in excellent agreement and the correlation coefficient is 0.94. (b) A profile showing MIGHTI-A and MIGHTI-B (MTA vs MTB) daytime temperature correlations

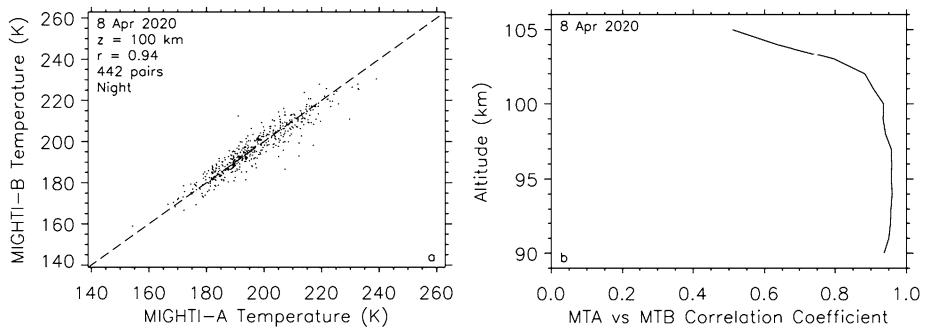
the difference is dominated by the uncertainty in the flat fields (3 K for each measurement at all altitudes) and at the upper altitudes (> 110 km) the bias is dominated by uncertainties in the temperatures above the highest observed tangent height, which are not measured, as discussed in Sect. 4.1.

Figure 24a shows the same comparison except for nighttime measurements. There are fewer profiles than for daytime conditions in Fig. 22 primarily because the integration time at night is twice as long as during the day. Figure 24b shows the difference between the averages, as well as the nighttime averages from three other days, spaced six months apart. Again, the differences are repeatable and generally within the estimated bias uncertainties.

Of particular relevance to the overarching science goals of ICON is the MLT temperature variability. To this end we directly compare the daytime temperatures from Fig. 22a interpolated to 100 km altitude in a scatterplot and show the result in Fig. 25a. It is evident that the MIGHTI-A and MIGHTI-B temperatures at this altitude are very similar with a very high correlation coefficient of 0.94. We also show a profile of correlation coefficients at all altitudes in Fig. 25b and, for the primary science region for MIGHTI from 90–105 km, they are all above 0.9.

Figure 26a shows the nighttime temperatures from Fig. 24a interpolated to 100 km altitude and compared again. Like the daytime temperatures, the correlation between the two is excellent ( $r=0.94$ ). The altitude profile of the correlation coefficients is similarly very good





**Fig. 26** (a) Same as Fig. 25a but for MIGHTI-A and MIGHTI-B nighttime temperatures. (b) Same as Fig. 25b but for nighttime temperatures

from 90–105 km. Figures 22–26 together demonstrate that MIGHTI-A and MIGHTI-B temperatures are not only in good absolute agreement, but are both measuring similar variations in the atmosphere. We next compare against extant observations from other instruments.

## 5 Comparison with Other Temperature Observations

### 5.1 Comparison with Satellite Observations

Currently, the most comprehensive global-scale dataset of MLT temperatures is that from the Sounding of the Atmosphere using Broadband Emission Radiometry (SABER) instrument (Russell et al. 1999) on NASA's Thermosphere, Ionosphere, Mesosphere, Energetics, and Dynamics (TIMED) mission. SABER has been operating since 2002 and the most recent version of the data (Remsberg et al. 2008) provides temperatures from 15–110 km altitude over all LT and latitudes observed by MIGHTI.

The SABER temperatures are derived from measurements of infrared emission from the vibration-rotation bands of carbon dioxide ( $\text{CO}_2$ ) at 15  $\mu\text{m}$ . In addition to the radiance measurements, the vertical profile of  $\text{CO}_2$  is required as an input to the temperature derivation algorithm. For the SABER v2.07 data product,  $\text{CO}_2$  is provided by the Whole Atmosphere Community Climate Model (WACCM) in which the  $\text{CO}_2$  abundance increases with time. Output from WACCM is routinely provided to the SABER processing team as time goes on.

In June 2022 the SABER team discovered that the  $\text{CO}_2$  profiles provided from the WACCM model beginning in late December 2019 and continuing to the present were from a different run of the WACCM model than had been previously used by SABER. This new run had a different set of specified parameters, most notably the Prandtl number, that resulted in much larger  $\text{CO}_2$  concentrations above 80 km than in the prior WACCM version used by SABER. As a consequence, the higher  $\text{CO}_2$  concentrations used in the SABER retrievals resulted in slightly lower temperatures from late December 2019 onward.

The SABER team has reprocessed the temperature data from December 2019 onward as of late June 2022 with WACCM data consistent with that used for the prior 18 years. These reprocessed v2.08 global mean temperatures are from 0.7 K to 5.3 K higher than the previous v2.07 temperatures over the range of  $1 \times 10^{-3}$  hPa (93 km) to  $1 \times 10^{-4}$  hPa (105 km) in 2020.

Because of the inherent temperature variability in the MLT (see Figs. 22 and 24) it is imperative to find close coincidences in both space and time between MIGHTI and SABER

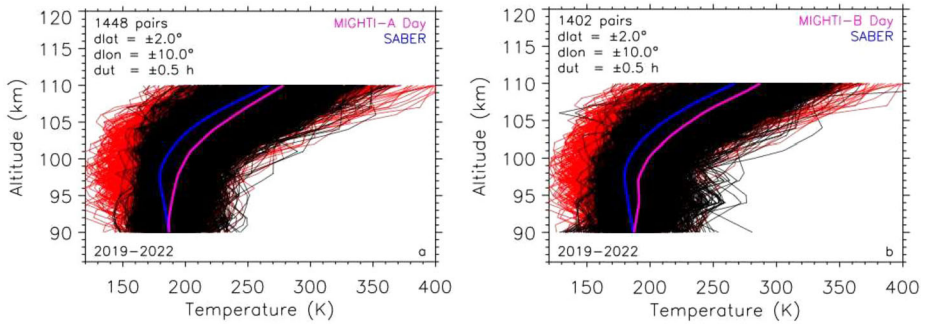


**Fig. 27** (a) Comparison of MIGHTI-A (black) and SABER (red) daytime profiles between December 2019 and February 2022. The MIGHTI average (magenta) and the SABER average (blue) are overlotted. Coincidence criteria for latitude, longitude, and UT are indicated as well as the total number of SABER-MIGHTI pairs. MIGHTI data are limited to solar zenith angles less than  $75^\circ$  to avoid the terminator. (b) Same as Fig. 27a except for MIGHTI-B and SABER daytime profiles

temperature profiles to properly quantify any persistent differences with altitude. Coincidence windows that are too small will result in only a small number of pairs, whereas windows that are too large will introduce other physical processes into the comparison such as diurnal or latitudinal variability. We have empirically determined that for the MIGHTI and SABER comparison a UT window of  $\pm 0.5$  h, a latitude window of  $\pm 2.0^\circ$ , and a longitude window of  $\pm 10.0^\circ$  allow for a sufficient number of profile pairs without introducing major geophysical variations to the comparison. We furthermore limit our daytime comparisons to those profiles with solar zenith angles less than  $75^\circ$  (greater than  $105^\circ$  for nighttime) to avoid the terminator. Our approach finds all SABER profiles that satisfy the above criteria for each MIGHTI profile.

These windows are separately applied to all MIGHTI-A data (day and night) and MIGHTI-B data (day and night) from 15 December 2019 through 11 February 2022. The daytime results comparing MIGHTI-A with SABER and MIGHTI-B with SABER are shown in Figs. 27a and 27b, respectively. Figure 27 shows that both MIGHTI-A and MIGHTI-B daytime temperatures are in excellent agreement with SABER temperatures between 90 and 95 km altitude (within 6 K on average). Above that, the differences become larger so that from 99 to 105 km both the MIGHTI-A and MIGHTI-B daytime temperatures are on average 18 K higher than SABER temperatures.

Figure 28 shows the comparison between MIGHTI-A and MIGHTI-B nighttime profiles with corresponding SABER profiles, using the same coincidence windows as for the daytime profiles. Figure 28 shows that MIGHTI-A and MIGHTI-B nighttime temperatures are within 7 K at all altitudes from 90 to 105 km.

The MIGHTI-SABER differences in Figs. 27 and 28 are better seen in Fig. 29, where we have taken the difference of the averages and show them for daytime in Fig. 29a and nighttime in Fig. 29b. We emphasize that the paired profiles for MIGHTI and SABER are separately found for MIGHTI-A day, MIGHTI-B day, MIGHTI-A night, and MIGHTI-B night. Figure 29 therefore serves to indicate that MIGHTI-A and MIGHTI-B are each providing consistent results when compared against SABER from December 2019 to February 2022.

Also shown in Fig. 29 is the result of adding the reported bias uncertainties for the SABER data ([saber.gats-inc.com/temp\\_errors.php](http://saber.gats-inc.com/temp_errors.php)) and the MIGHTI data (see Fig. 23). Due to the large number of profile pairs, which essentially eliminates the statistical uncertainties,

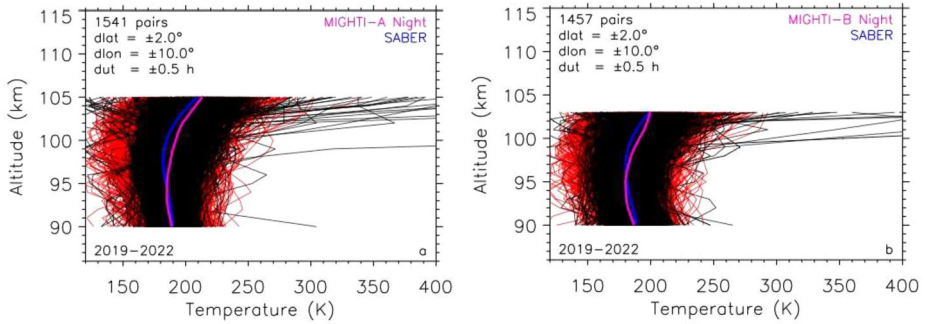


**Fig. 28** (a) Same as Fig. 27a except for MIGHTI-A and SABER nighttime profiles. MIGHTI data are limited to solar zenith angles greater than  $105^\circ$  to avoid the terminator. (b) Same as Fig. 27b except for MIGHTI-B and SABER nighttime profiles

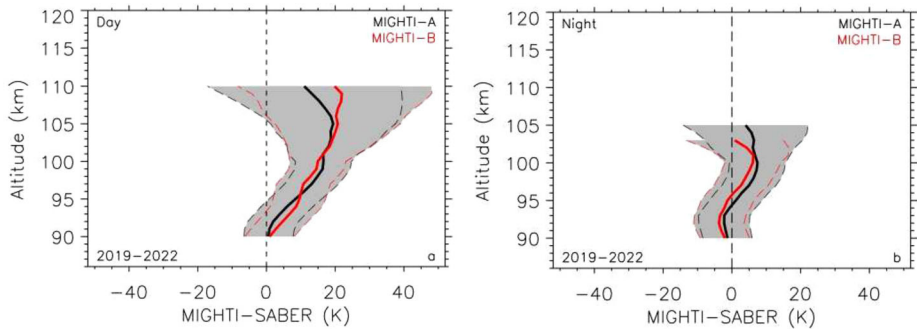


**Fig. 29** (a) Differences of MIGHTI-A (black) and MIGHTI-B (red) daytime temperature profiles in Fig. 27 with corresponding SABER temperature profiles. The combined systematic uncertainties, bounded by the dashed lines are added together linearly and shown as the shaded area. (b) Same as Fig. 29a except for nighttime profiles

the only uncertainty used in this comparison is the bias (or systematic) uncertainty for each dataset. Reported systematic uncertainties for SABER temperatures are 4 K at 90 km and increase to 25 K at 110 km. These uncertainties include both the effects of absolute calibration as well as any uncertainties in the temperature retrieval algorithm. Estimated biases are the same for both SABER and MIGHTI during daytime and nighttime. Figure 29a shows that daytime differences are within the combined systematic uncertainties up to  $\sim 95$  km but are greater than the combined uncertainties above that, although near the top of the comparison shown at 110 km altitude the differences are again within the combined uncertainty. Figure 29b shows that nighttime differences are completely within the combined uncertainty of the two sets of observations for MIGHTI-A and MIGHTI-B.

### 5.2 Comparison with Ground-Based Observations

We also compare daytime MIGHTI temperature profiles against a ground-based dataset. Daytime temperature measurements in the MLT from ground-based instruments are scarce. During a special campaign at Utah State University (USU) ( $41.7^\circ$  N,  $111.8^\circ$  W), the USU sodium (Na) Doppler lidar operated in daytime for nine days between 26 February and 2 April 2021, providing an opportunity to compare against concurrent MIGHTI daytime temperature measurements. By taking advantage of the mesospheric Na layer ( $\sim 80$ – $105$  km),

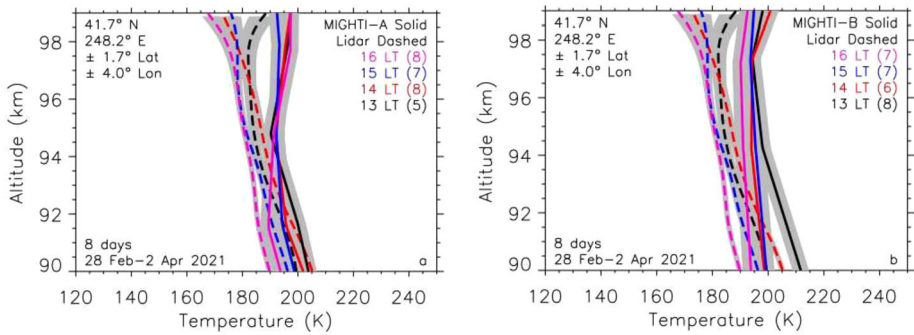


**Fig. 30** (a) Comparisons of daytime temperature profiles between the USU Na lidar and MIGHTI-A four afternoon hours between 13 LT and 16 LT. The temperature profiles with the same color represent the observations during the same hour by the two instruments. The number of MIGHTI profiles for each hourly profile are indicated in parentheses. (b) Same as Fig. 30a except for MIGHTI-B temperature profiles

the Na Doppler lidar technique measures the thermal broadening (temperature) and Doppler shift (bulk motion) of the metallic Na atoms in the MLT region (Krueger et al. 2015). Its daytime capability is enabled by a unique Faraday filter deployed in the lidar receiver (Harrell et al. 2009) that rejects the majority of the sky background, while allowing the lidar echoes to pass through. The Na lidar uncertainty depends primarily on the photon shot-noise ( $\leq 10$  K), particularly during the daytime at the top of the profiles near 99 km (Yuan et al. 2009). Comparisons of an earlier version (v04) of MIGHTI daytime data during this campaign were presented by Yuan et al. (2021) and showed agreement to within 7 K in the same altitude region and for the same time period.

Figures 30a and 30b illustrate the comparisons of the average temperature profiles of four different hours in the afternoon between the lidar results and the MIGHTI-A and MIGHTI-B results, respectively. In this work, both the MIGHTI-A and MIGHTI-B observations within  $\pm 1.7^\circ$  latitude and  $\pm 4.0^\circ$  longitude are selected and binned hourly for each local/universal time during the lidar campaign. Each lidar profile is the average of all the lidar measurements within this hour over the campaign. In these figures, the average uncertainties of the lidar temperatures are 4 K at 90 km and 10 K at 99 km, respectively. Although the results for individual LT bins are similar, the number of profiles for each LT (shown in the panels) is limited, ranging from 5 to 8 over nine days during the indicated time period.

Overall, within the overlapping altitude range 90–99 km, the temperature difference between the two instruments increases with altitude. In general, the two sets of temperatures are within 7 K on average over all LT between 90–95 km for either MIGHTI-A or MIGHTI-B. From 95–99 km the differences grow to more than 20 K for some LT for both MIGHTI-A and MIGHTI-B, with MIGHTI temperatures consistently higher than the lidar temperatures. This difference is shown more clearly in Fig. 31 by subtracting the hourly averaged lidar profiles from the corresponding averaged MIGHTI-A and MIGHTI-B profiles. The daytime differences with the lidar results in Fig. 31 are similar to daytime differences shown from 90–99 km in Fig. 29 for the SABER comparison.

## 6 Discussion

Our analysis reveals that there is good agreement between MIGHTI-A and MIGHTI-B temperatures throughout the day, as shown in Figs. 22 and 24. This agreement is despite the

**Fig. 31** Differences of MIGHTI-A (solid) and MIGHTI-B (dashed) profiles from Fig. 29. The shaded region shows the root-sum-square statistical uncertainty for the average lidar profiles (4–10 K) and the systematic uncertainty for the MIGHTI profiles (about 3 K). Hourly averaged profiles are indicated by the different colors

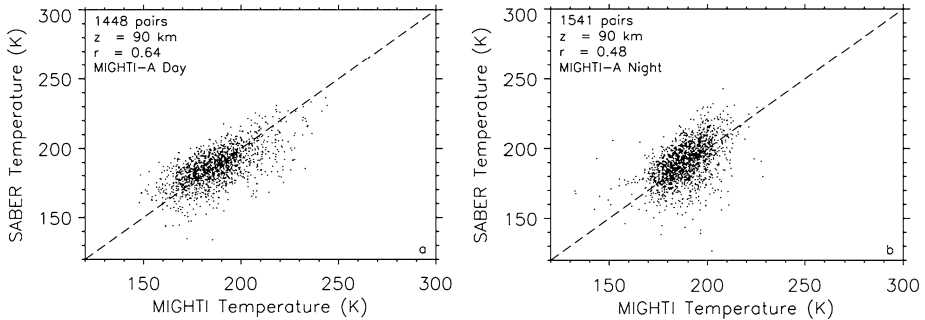
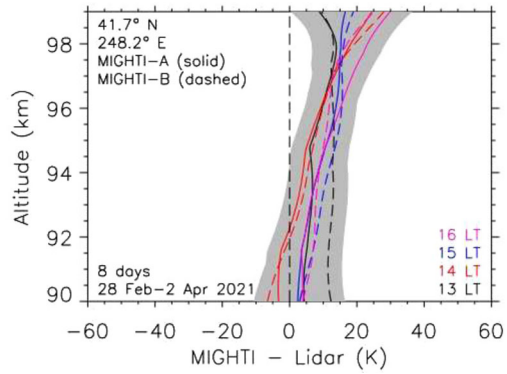


**Fig. 32** (a) Comparison of daytime temperatures for pairs of observations from MIGHTI-A and SABER at 90 km during the daytime. Coincidence criteria are the same as shown in Fig. 27. (b) Same as Fig. 32a except for nighttime temperatures

fact that the MIGHTI-A and MIGHTI-B observations are nine minutes apart and view the tangent point from orthogonal look directions. The agreement is particularly compelling because the relative responsivities (see Figs. 6 and 7), as well as the on-orbit modifications to both the responsivities and the channel wavelengths described in Sect. 3 are nearly independently determined to achieve internal channel consistency, and are specific to MIGHTI-A day, MIGHTI-B day, MIGHTI-A night, and MIGHTI-B night. More importantly and central to the science objectives of ICON, there is excellent agreement between MIGHTI-A and MIGHTI-B temperature variability as shown in Figs. 25 and 26, where correlation coefficients are near unity from 90–100 km throughout the day.

Relative variations are shown by a comparison of MIGHTI-A daytime temperatures with SABER at 90 km in Fig. 32a and nighttime temperatures in Fig. 32b. Correlation coefficients are smaller (0.48–0.64) than the MIGHTI-A and MIGHTI-B comparisons shown in Fig. 25, but the coincidence windows shown in the upper left are greater than the MIGHTI-A vs. MIGHTI-B coincidences ( $\pm 0.50$  h in UT compared to 0.15 h, for example) so we would expect them to be less. We also show dashed reference lines in Fig. 32 indicating where MIGHTI and SABER would yield the same temperature. At this altitude, the observations are scattered predominantly around this line for both daytime and nighttime conditions underscoring the good agreement in absolute temperature at 90 km.

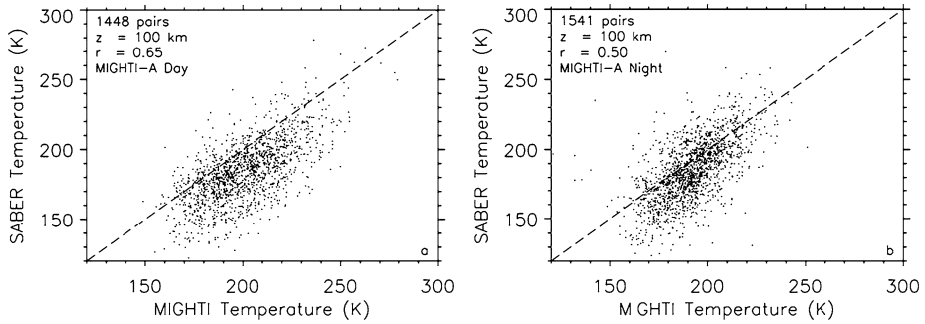


**Fig. 33** (a) Comparison of daytime temperatures for pairs of observations from MIGHTI-A and SABER at 100 km during the daytime. Coincidence criteria are the same as shown in Fig. 28. The correlation coefficient ( $r$ ) between the MIGHTI and SABER temperatures is indicated. (b) Same as Fig. 33a except for nighttime temperatures

A scatterplot of MIGHTI-A temperatures against SABER temperatures is shown for a 100 km altitude in Fig. 33a for daytime conditions and Fig. 33b for nighttime conditions. In this case one can see that the MIGHTI-A temperatures are systematically higher than the SABER temperatures, particularly during the daytime as discussed, where the MIGHTI-A temperatures are nearly 20 K higher than SABER temperatures.

We consider the possibility here that SABER temperature biases may play a role in the differences shown in Fig. 29. Potential SABER temperature errors from 90–110 km have been discussed by Mertens et al. (2001), Remsberg et al. (2008), Garcia-Comas et al. (2008), Rezac et al. (2015), and Dawkins et al. (2018) and are reflected in the combined MIGHTI and SABER uncertainties shown in Fig. 29. The behavior of the MIGHTI-SABER differences with altitude shown in Fig. 29 rules out a radiometric calibration error in SABER as a cause of the differences, which has moreover been shown to be stable in an independent study (Mlynczak et al. 2020). Nonetheless, the day-night differences shown in Fig. 29 could lead to differences in, for example, the derived amplitude of the diurnal migrating tide from both instruments, so the reader is cautioned when comparing this amplitude as a function of altitude between the temperature datasets.

Two constituents required for the SABER temperature retrieval that become important at these altitudes are the carbon dioxide ( $\text{CO}_2$ ) concentration and the atomic oxygen (O) concentration. Although the daytime temperature differences are larger than the nighttime differences, the increase in the differences with altitude have a similar shape from 90–100 km suggesting that the rates of collisional quenching and excitation of  $\text{CO}_2$  vibrational states by O may play a role. This rate is the most critical of the non-LTE processes that give rise to 15  $\mu\text{m}$  emission by  $\text{CO}_2$  observed by SABER.  $\text{CO}_2$  and O furthermore exhibit a vertical gradient in concentration for this altitude region, which means that their abundances will vary with time of day due to tides. The effect of uncertainty in O on the retrieved SABER temperatures is such that the O used in the SABER retrieval at 110 km would have to be about 50% larger than was actually in the atmosphere in order to realize the entire MIGHTI-SABER difference observed. It is beyond the scope of this paper to reconcile the absolute MIGHTI-SABER temperature differences shown in Fig. 29 and leave that work for another study. Note that the SABER temperature retrievals above  $\sim 100$  km uses O from the NRLMSISE-00 empirical model, which has since been improved Emmert et al. (2020).

## 7 Summary

We have presented the methodology used in retrieving v05 temperatures from O<sub>2</sub> A-band observations using two different sensors for the MIGHTI instrument on the NASA ICON satellite. This methodology includes unique on-orbit observations of the Rayleigh scattered background in two background channels that enable improvements to pre-flight measurements of the relative responsivity. The three on-band MIGHTI signal channels for each sensor furthermore allow for small improvements to the pre-flight measurements of channel wavelengths, allowing for self-consistency between the channels. These improvements yield two independent, concurrent, and self-consistent sets of temperature profiles throughout the diurnal cycle from 90–127 km during the day and 90–108 km at night.

The MIGHTI temperatures are compared to temperature observations from the NASA SABER instrument as well as daytime ground-based Na lidar observations. MIGHTI-A and MIGHTI-B are on average within 7 K of these independent observations from 90 to 95 km throughout the day and night. The differences in the daytime gradually become larger with increasing altitude until MIGHTI-A and MIGHTI-B temperatures are both on average 18 K higher than SABER temperatures between 99–105 km. In the nighttime the MIGHTI and SABER temperature differences are within the combined systematic uncertainties of the two instruments at all altitudes from 90 to 105 km. Temperature variations about the mean are similar for MIGHTI-A, MIGHTI-B, and SABER so that most analyses that are based on variations at a given altitude are not affected by these systematic differences.

**Acknowledgements** We thank the entire NASA ICON team for many useful discussions from which this work benefited. We also thank to J.T. Emmert for many valuable discussions on other MLT temperature observations.

**Funding** ICON is supported by NASA's Explorers Program through contracts NNG12FA45C and NNG12FA421. The sodium lidar work was supported by NSF AGS 2125712.

**Data Availability** This study uses v05 Level 2.3 ICON-MIGHTI temperature data, which is available from the ICON website (<https://icon.ssl.berkeley.edu/Data>) and at the Space Physics Data Facility (<https://spdf.gsfc.nasa.gov/>).

## Declarations

**Competing Interests** The authors declare no competing interests.

**Open Access** This article is licensed under a Creative Commons Attribution 4.0 International License, which permits use, sharing, adaptation, distribution and reproduction in any medium or format, as long as you give appropriate credit to the original author(s) and the source, provide a link to the Creative Commons licence, and indicate if changes were made. The images or other third party material in this article are included in the article's Creative Commons licence, unless indicated otherwise in a credit line to the material. If material is not included in the article's Creative Commons licence and your intended use is not permitted by statutory regulation or exceeds the permitted use, you will need to obtain permission directly from the copyright holder. To view a copy of this licence, visit <http://creativecommons.org/licenses/by/4.0/>.

## References

- Babcock HD, Herzberg L (1948) *Astrophys J* 108:167
- Brasseur G, Solomon S (1986) *Aeronomy of the middle atmosphere*, 2nd edn. Reidel, Dordrecht, p 107
- Christensen AB et al (2012) *J Geophys Res* 117:A04315. <https://doi.org/10.1029/2011JA016838>
- Christensen AB et al (2013) *J Geophys Res* 118:3740. <https://doi.org/10.1002/jgra.50317>

- Dawkins ECM et al (2018) *J Geophys Res* 123:9916. <https://doi.org/10.1029/2018JD028742>
- Emmert JT et al (2020) *Earth Space Sci* 8:e2020EA001321. <https://doi.org/10.1029/2020EA001321>
- England SL (2012) *Space Sci Rev* 168:211. <https://doi.org/10.1007/s11214-011-9842-4>
- Englert CR et al (2007) *Appl Opt* 46:7297
- Englert CR et al (2017) *Space Sci Rev* 168:211. <https://doi.org/10.1007/s11214-017-0358-4>
- Forbess JM (1982) *J Geophys Res* 87:5222
- Garcia-Comas M et al (2008) *J Geophys Res*. <https://doi.org/10.1029/2008JD010105>
- Gordon IE et al (2017) *J Quant Spectrosc Radiat Transf* 203:3. <https://doi.org/10.1016/j.jqsrt.2017.06.038>
- Greer RGH et al (1981) *Planet Space Sci* 29:383
- Gumbel J et al (2020) *Atmos Chem Phys*. <https://doi.org/10.5194/acp-20-431-2020>
- Hagan ME et al (2007) *Geophys Res Lett*. <https://doi.org/10.1029/2007GL030142>
- Harding BJ et al (2017) *Space Sci Rev* 212:585. <https://doi.org/10.1007/s11214-017-0359-3>
- Harding BJ et al (2021) *J Geophys Res* 126:e2020JA028947. <https://doi.org/10.1029/2020JA028947>
- Harlander JM et al (1992) *Astrophys J* 396:730
- Harlander JM et al (2017) *Space Sci Rev* 212:601. <https://doi.org/10.1007/s11214-017-0374-4>
- Harrell SD et al (2009) *J Opt Soc Am B* 26:659. <https://doi.org/10.1364/JOSAB.26.000659>
- Harrison AW, Vallance Jones A (1957) *J Atmos Sol-Terr Phys* 11:192
- Heller JW et al (1991) *J Geophys Res* 96:19499
- Immel TJ et al (2009) *Earth Planets Space* 61:505. <https://doi.org/10.1186/BF03353167>
- Immel TJ et al (2018) *Space Sci Rev* 212:60. <https://doi.org/10.1007/s11214-017-0449-2>
- Kaufmann M et al (2018) *Atmos Meas Tech* 11:3861. <https://doi.org/10.5194/amt-11-3861-2018>
- Krueger DA et al (2015) *Appl Opt* 54:9469. <https://doi.org/10.1364/AO.54.009469>
- Liu G (2006) Ph.D. Dissertation, York University, Toronto, Ontario, Canada
- Liu G, Shepherd GG (2006) *Geophys Res Lett* 33:L09805. <https://doi.org/10.1029/2005GL025297>
- Llewellyn EJ et al (2004) *Can J Phys* 82:411. <https://doi.org/10.1139/p04-005>
- Markwardt CB (2009) In: Bohlender D, Dowler P, Durand D (eds) *Proc astron data analysis software and system XVIII*, vol 411, p 251
- Marsh DR et al (2006) *J Geophys Res* 111:A10S05. <https://doi.org/10.1029/2005JA011451>
- Mertens CJ et al (2001) *Geophys Res Lett* 28:1391. <https://doi.org/10.1029/2000GL012189>
- Mlynczak MG et al (2020) *Earth Space Sci* 7:e2019EA001011. <https://doi.org/10.1029/2019EA001011>
- Osterbrock DE et al (1996) *Astron Soc Pac* 108:277
- Remsberg EE et al (2008) *J Geophys Res* 113:D17101. <https://doi.org/10.1029/2008JD010013>
- Rezac L et al (2015) *J Atmos Sol-Terr Phys* 130:23. <https://doi.org/10.1016/j.jastp.2015.05.004>
- Russell JM III et al (1999) *SPIE J* 3756:277
- Sagawa E et al (2005) *J Geophys Res* 110:11302. <https://doi.org/10.1029/2004JA010848>
- Sheese PE et al (2010) *Can J Phys* 88:919. <https://doi.org/10.1139/p10-093>
- Skinner WR, Hays PB (1985) *Planet Space Sci* 1:17
- Slanger TG et al (2003) *J Geophys Res* 108:1293. <https://doi.org/10.1029/2003JA009885>
- Slanger TG et al (2017) *J Geophys Res* 122:3640. <https://doi.org/10.1002/2016JA023502>
- Stevens MH et al (2018) *Space Sci Rev* 214:4. <https://doi.org/10.1007/s11214-017-0434-9>
- Strickland DJ et al (1999) *J Quant Spectrosc Radiat Transf* 62:689
- Thuillier G et al (2003) *Sol Phys* 214:1. <https://doi.org/10.1023/A:1024048429145>
- Yee JH et al (1997) *J Geophys Res* 102:19,949
- Yee JH et al (2012) *Can J Phys* 90:769. <https://doi.org/10.1139/p2012-073>
- Yuan T et al (2009) *Appl Opt* 48:3988
- Yuan T et al (2021) *J Geophys Res* 126:e2021JD035321. <https://doi.org/10.1029/2021JD035321>

**Publisher's Note** Springer Nature remains neutral with regard to jurisdictional claims in published maps and institutional affiliations.